Hidden traces of chirality in the fluctuations of a fully unwound cholesteric

Guilhem Poy

▶ To cite this version:

Guilhem Poy. Hidden traces of chirality in the fluctuations of a fully unwound cholesteric. Soft Matter, 2023, 19 (6), pp.1115-1130. 10.1039/D2SM01646J . hal-03953472

HAL Id: hal-03953472
https://hal.science/hal-03953472v1

Submitted on 24 Jan 2023

HAL is a multi-disciplinary open access archive for the deposit and dissemination of scientific research documents, whether they are published or not. The documents may come from teaching and research institutions in France or abroad, or from public or private research centers.

L'archive ouverte pluridisciplinaire **HAL**, est destinée au dépôt et à la diffusion de documents scientifiques de niveau recherche, publiés ou non, émanant des établissements d'enseignement et de recherche français ou étrangers, des laboratoires publics ou privés.

Public Domain

Soft Matter

ARTICLE TYPE

Cite this: DOI: 00.0000/xxxxxxxxxx

Hidden traces of chirality in the fluctuations of a fully unwound cholesteric†

Guilhem Poy*[a]

Received Date
Accepted Date

DOI: 00.0000/xxxxxxxxxx

Confinement and hydrodynamic interactions often play an important role in the fluctuation dynamics of soft matter systems, which can typically be studied using light scattering techniques. With experimental and theoretical methodologies, I demonstrate here that chirality is an additional critical parameter that leads to diverging decay times and correlation lengths in chiral liquid crystal cells with a fully unwound cholesteric helix. This study combines light scattering measurements made in a tailored microscope geometry and theoretical calculations of the decay dynamics of chiral orientational fluctuations—including hydrodynamics—to establish the existence of two soft chiral modes of fluctuations driving the destabilization of the unwound cholesteric. Despite the achirality of the equilibrium state of unwound cholesterics, this study indicates that chirality hides itself in the orientational fluctuation modes and plays a major role in their dynamics, which can be exploited to locally measure the strength of chirality in frustrated chiral liquid crystal cells.

1 Introduction

Thermal fluctuations are a prevalent feature of soft matter systems and often unveil many details about the structure and dynamics of a given material using light scattering techniques[1,2]. An emblematic example is the thermally-induced Brownian motion of particles in a dilute colloidal suspension. With dynamic light scattering (DLS), light interacts with the fluctuating particles and allows the measurement of the temporal correlation of the fluctuations, which typically decays exponentially with a diffusive-like decay frequency proportional to the Brownian diffusion coefficient and the squared scattering wavevector. Using the Stokes-Einstein relation, these measurements give information about the hydrodynamics radius of the particles or the viscosity of the fluid.

Beyond the measurement of the hydrodynamic radius in dilute colloidal suspensions, light scattering is also very valuable to study the dynamics of other soft systems such as jammed materials[3,4], microgels[5,6], proteins[7,8], and liquid crystals[9] (LCs). In nematic LCs, the orientational fluctuations of the elongated LC molecules are the slowest decaying modes and allow experimentalists to fully characterize the elastic and viscous properties of the LC[10,11] and more subtle phenomena such as surface dissipation in highly confined cylindrical pores[12], critical slowing down near the optical Freedericksz transition threshold[13], and couplings with hydrodynamic flows in confined cells[14]. In addition to the simple nematic phase, DLS techniques were also used to reveal the fascinating multiscale dynamics of more complicated phases such as twist-bend nematics[15] and confined blue phase III[16]. The latter phase is intrinsically chiral and is closely related to the chiral nematic phase, also called the cholesteric phase. In these chiral LC phases, chirality induces twisted equilibrium structures characterized by a wavevector q called the spontaneous twist. These twisted structures strongly interact with both light and orientational fluctuations, leading for example to a critical divergence of experimentally observed decay times in cholesterics[17] at scattering wavevectors equal to $\pm 2q$, thus showing again the deep link between structure and dynamics in fluctuating physical systems. On a similar note, Jia *et al.* showed that chirality was drastically changing the shape of the fluctuation spectrum associated with the edge of smectic colloidal membranes[18].

In the aforementioned LC studies, confinement often plays a critical role in the dynamics of the fluctuation modes, leading to reduced hydrodynamic fluctuations due to no-slip boundaries or strong structural and dynamic tuning of the orientational modes due to the interaction with the alignment layers of the sample. Intriguingly, such effects of confinement on thermal fluctuations were, to the best of my knowledge, never explored in cholesterics. This is surprising, to say the least, since confined cholesterics are an archetypal example of a frustrated system in which the equilibrium state of the unconfined phase—the equilibrium cholesteric helix—cannot form due to the conflicting anchoring boundary conditions of LC molecules near the confining surfaces. This frustration typically leads to deep structural changes in the LC orientational field, with a complete zoology of localized and/or

---

[a] *L2C, Univ Montpellier, CNRS, Montpellier, France. Tel: +33 4 67 14 42 84; E-mail: guilhem.poy@umontpellier.fr*

† Electronic Supplementary Information (ESI) available for additional experimental and theoretical data. See DOI: `https://doi.org/10.1039/D2SM01646J`.

periodic LC patterns existing on top of a translationally invariant background, such as cholesteric fingers and bubbles[19], heliknotons[20], hopfions and more complicated examples of these so-called topological solitons[21]. The stability diagram of such patterns shows several structural transitions due to a delicate balance between the twist-suppressing action of confinement and the twist-favouring action of chirality. One may rightfully wonder if the same balance affects the structure and dynamics of the orientational fluctuations in these frustrated chiral systems since phase transitions are often accompanied by pretransitional critical phenomena.

The goal of this paper is to provide the first step toward a better understanding of the fluctuating dynamics of chiral frustrated systems by focusing on the simplest type of confined cholesterics, namely unwound cholesterics obtained by confining the LC between two plates imposing a molecular alignment normal to their surfaces. Below a critical thickness that depends on q, the most stable state of such systems is the so-called unwound helix, corresponding to a complete suppression of the cholesteric twist in the bulk with a uniform alignment of all LC molecules normal to the sample plates.

First, I describe a light scattering microscope setup tailored to the study of LC fluctuation modes with very small scattering wavevectors and use this setup to experimentally demonstrate the existence of a soft chiral fluctuation mode whose decay frequency becomes vanishingly small as the threshold of destabilization of the unwound cholesterics is approached (Sec. 2). I then present a complete theory of the decay dynamics of confined chiral fluctuations in unwound cholesterics (Sec. 3) and examine in more detail my experimental results in light of this model (Sec. 4). Finally, conclusions and extensions of this work are discussed in Sec. 5.

2 Experimental evidence of a chiral soft fluctuation mode

2.1 Experimental setup and methods

The samples of this study were assembled from two parallel glass plates separated with UV glue lines containing calibrated colloidal spacers of diameter $\sim 11\,\mu$m. Before assembly, I systematically washed the glass plates with distilled water, acetone and ethanol in a sonicator, and chemically treated them to ensure homeotropic anchoring. To perform this surface treatment, I prepared a solution of 90 wt% ethanol, 10 wt% ultrapure water and 0.1 wt% DMOAP (dimethyloctadecyl[3-(trimethoxysilyl)propyl]ammonium chloride, Sigma Aldrich), filtered and deposited this solution by spin-coating at 2000 rpm during 20 s on the glass plates, which were finally baked at 110 °C during 1 h. All samples were filled by capillarity with cholesteric mixtures of the nematic 5CB (4-cyano-4'-*n*-pentylbiphenyl, Synthon Chemicals) doped with a mass fraction C of the chiral molecule R811 (R-[+]-octan-2-yl 4-[{4-(hexyloxy)benzoyl}-oxy]benzoate, BLD Pharmatech). Before filling any sample, its thickness is mapped with a spectrometer mounted on a microscope with an XY translation stage, based on reference scratches made with a diamond on the side of the sample. This way, any local observation of the same sample under a microscope can be accurately associated with the local value of the sample thickness (typically ranging from 10 to 12 μm) even if the plates are not perfectly parallel (typical tilt angle < 0.3 mrad). In addition, I measured the helical twist power (HTP) of the mixtures of 5CB and R811 with the Cano wedge method, as detailed in the ESI†. I found that $\text{HTP} \equiv q/(2\pi C) = 0.1155\,\text{wt}\%^{-1}\mu\text{m}^{-1}$ at a temperature 5° below the nematic/isotropic transition temperature T_{NI}, with $q = 2\pi/P$ the spontaneous twist of the cholesteric phase and P the equilibrium pitch of an unconfined cholesteric helix.

Each sample is observed under crossed polarisers with a Leica DM2500P polarized optical microscope (POM). The temperature of the sample is regulated within 0.1 °C with an Instec STC200 temperature controller and oven, and the horizontal position of the sample can be adjusted with an XY translation stage. To optimize the contrast of the thermal orientational fluctuations, the sample stage holder imposes a small angle of $\theta \sim 5°$ in the y direction (at 45° with respect to the polarisers) as schematized in Fig. 1a. This technical point will be further discussed in the next subsection. The sample is illuminated with broad spectrum LED light from a CoolLED pE-300 white lamp and observed by an sCMOS camera (Andor Zyla) through a x10 objective with a 0.25 numerical aperture. Typical acquisitions are done on a square region of interest of 256 pixels (166.9 μm) at a framerate of 100 or 200 Hz, with a dynamic range of 4096 (12-bit pixel data). I performed all acquisitions with the condenser aperture closed as much as possible, so that one can assume that the incident light is propagating along the axis $\boldsymbol{e}'_z$ of Fig. 1a. All error bars in this paper are estimated as 3× the standard deviation of a given quantity (calculated either from the covariance matrix of a fit or the sample standard deviation of a noisy dataset), which corresponds to a confidence level of $\sim 99.7\,\%$ assuming Gaussian randomness.

2.2 Choice of dynamic differential microscopy geometry

The main experimental technique of this paper is Dynamic Differential Microscopy (DDM), which allows the measurement of the static and dynamic properties of all fluctuation modes with moderate scattering wavevectors $\boldsymbol{k}_\perp$ from a single microscope movie. Giavazzi *et al.*[22] proposed several DDM geometries to characterize the material constants of LCs, but unfortunately, these geometries are not optimal for the goal of this paper since we want to target fluctuation modes with a vanishingly small scattering wavevector, for which these previous setups lead to a poor optical contrast in the case of homeotropic samples. To better understand this, let us estimate the scattering cross-section of the setup in Fig. 1a, assuming general orientations of the polariser and analyser. Since the fluctuation modes are confined in the thickness of the sample, we can expect that modes with in-sample-plane wavevectors $\boldsymbol{k}_\perp$ are the dominant contribution to the scattering cross-section[23], i.e. $\boldsymbol{k}_\perp$ is in the xy plane of Fig. 1a. De Gennes calculated the differential contribution $S(\boldsymbol{k}_\perp)$ of a mode with wavevector $\boldsymbol{k}_\perp$ to the total scattering cross-section (see Sec. 3.4.3 in Ref.[24]), but his calculation only applies to DLS setup with the polariser (analyser) orthogonal to the incident (scattered) beam. This is not the case of the microscope setup in Fig. 1a, since a

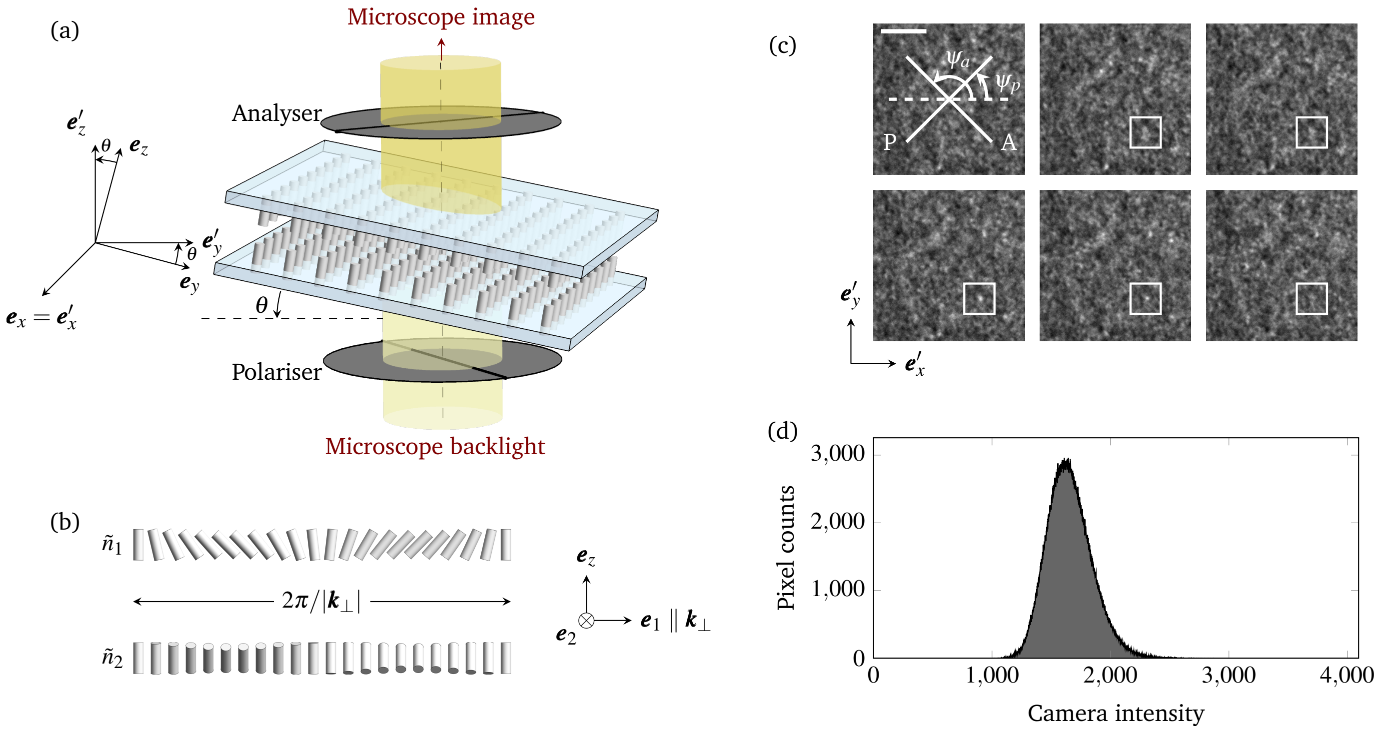

Fig. 1 (a) Schematic of the polarized optical microscope (POM) setup. Light propagates along z' (central axis of the microscope) and the microscope polarisers are parallel to the $x'y'$ plane. The rotated coordinate system (x,y,z) associated with the sample has its z direction along the alignment direction of the unperturbed director field. (b) Schematics of the two types of director fluctuation in a nematic LC, either parallel or orthogonal to the fluctuation wavevector $\boldsymbol{k}_\perp$. These fluctuations are the splay-bend and twist-bend modes described later in this paper. (c) Snapshots of a typical acquisition made in a nematic sample of 5CB. Time increases from 10 ms between each image, from left to right along the top row, and then along the bottom row. The image contrast was enhanced to better visualize the intensity fluctuations. The definition of the polariser (P) angle ψ_p and analyser (A) angle ψ_a is shown in the top left image, and the white square indicate a region where a bright intensity fluctuation is created and then destroyed. The white bar represents 50 µm. (d) Raw intensity histogram of the whole acquisition in (c).

nonzero $\boldsymbol{k}_\perp$ is associated with an off-axis scattered field on the analyser, the latter being always parallel to the xy plane. Fortunately, De Gennes's formula is generalized in a straightforward manner as follows:

$$\frac{S(\boldsymbol{k}_\perp)}{\sigma_0} = \sum_{j=1,2} \left[\left(\boldsymbol{p}\cdot\boldsymbol{e}_j\right)\left(\tilde{\boldsymbol{a}}\cdot\boldsymbol{e}_z\right) + \left(\boldsymbol{p}\cdot\boldsymbol{e}_z\right)\left(\tilde{\boldsymbol{a}}\cdot\boldsymbol{e}_j\right)\right]^2 \left\langle |\tilde{n}_j(\boldsymbol{k}_\perp)|^2 \right\rangle \quad (1)$$

In the latter formula, $\sigma_0 = [\varepsilon_a k^2/(4\pi)]^2$ is a constant defined in terms of the anisotropy of permittivity ε_a and the wavevector of light $k = 2\pi n_o/\lambda_0$, with n_o the LC ordinary refractive index and λ_0 the wavelength in empty space. $\langle |\tilde{n}_j(\boldsymbol{k}_\perp)|^2 \rangle$ corresponds to the statistical average of the squared amplitude of the j-th fluctuation eigenmode with Fourier wavevector $\boldsymbol{k}_\perp$. For the sake of simplicity, we assume here that the sample is only weakly chiral, which implies (see Sec. 3.4.2 in Ref.[24]) that the first (second) eigenmode can be chosen as a director perturbation parallel (orthogonal) to $\boldsymbol{k}_\perp$ and associated with the unit vectors $\boldsymbol{e}_1 \equiv \boldsymbol{k}_\perp/|\boldsymbol{k}_\perp|$ and $\boldsymbol{e}_2 \equiv \boldsymbol{e}_z \times \boldsymbol{e}_1$, as in nematics. These director perturbations are schematized in Fig. 1b. The unit-normed vector orientation of the polariser was defined as $\boldsymbol{p} \equiv \cos\psi_p \boldsymbol{e}'_x + \sin\psi_p \boldsymbol{e}'_y$, with the angle ψ_p defined in Fig. 1c. The modified orientation of the analyser $\tilde{\boldsymbol{a}}$—not used in De Gennes's original formula—was obtained using the approach of Korger *et al.*[25], who defined a generalized projection operator for off-axis optical fields incident on a polariser made of anisotropic and absorbing nanoparticles. It can be calculated from the unit-normed vector orientation of the analyser $\boldsymbol{a} \equiv \cos\psi_a \boldsymbol{e}'_x + \sin\psi_a \boldsymbol{e}'_y$ (with the angle ψ_a defined in Fig. 1c) as follows:

$$\tilde{\boldsymbol{a}} \equiv \boldsymbol{a} + \frac{\boldsymbol{k}'_\perp \cdot \boldsymbol{a}}{k} \boldsymbol{e}'_z, \quad (2)$$

with $\boldsymbol{k}'_\perp \equiv k_x \boldsymbol{e}'_x + (k_y/\cos\theta)\boldsymbol{e}'_y$. All these formulas were simplified in the paraxial limit of small $|\boldsymbol{k}_\perp|/k$, which is justified since the numerical aperture of our microscope objective is small. In De Gennes's original formula, $\boldsymbol{a}$ is used instead of the generalized projection direction $\tilde{\boldsymbol{a}}$, which, in our setup, is only valid if $\boldsymbol{k}_\perp = \boldsymbol{0}$ (scattered field normal to the analyser).

We can now develop eqn (1) in two limit cases. Let us consider first the geometries introduced by Giavazzi *et al.*[22]. With the notations of this paper, these geometries correspond to $\theta = 0$ (untilted sample), and up to a global rotation around $\boldsymbol{e}_z$, $\psi_p = 0$ and $\psi_a = \psi$, with $\psi = 0$ ($\psi \neq 0$) in geometry "H1" (geometry "H2") of Ref.[22]. With these values, eqn (1) simplifies to:

$$S(\boldsymbol{k}_\perp) = \sigma_0 \frac{|\boldsymbol{k}_\perp|^2}{k^2} \begin{cases} \cos^2\psi \langle |\tilde{n}_1(\boldsymbol{k}_\perp)|^2 \rangle & \text{if } \boldsymbol{k}_\perp \parallel \boldsymbol{e}_x \\ \sin^2\psi \langle |\tilde{n}_2(\boldsymbol{k}_\perp)|^2 \rangle & \text{if } \boldsymbol{k}_\perp \parallel \boldsymbol{e}_y \end{cases} \quad (3)$$

This calculation reproduces the conclusion of Giavazzi *et al.*, namely that in these geometries one can select one of the two fluctuation eigenmodes with the scattering wavevector along the x or

y axis as soon as ψ is different from 0 and $\pi/2$. However, the scattered field intensity scales as $|\boldsymbol{k}_\perp|^2/k^2$, which means that forward-scattering modes with $\boldsymbol{k}_\perp = \boldsymbol{0}$ cannot be observed in these setups.

Let us consider now a new experimental setup by imposing $\theta \neq 0$ (tilted sample), $\psi_p = \pi/4$ and $\psi_a = 3\pi/4$ (crossed polarisers symmetric with respect to $\boldsymbol{e}'_y$). With these values and assuming that $|\boldsymbol{k}_\perp| \ll k\sin 2\theta$, eqn (1) simplifies to:

$$S(\boldsymbol{k}_\perp) = \sigma_0 \left[\frac{\sin(2\theta)}{2}\right]^2 \begin{cases} \langle|\tilde{n}_2(\boldsymbol{k}_\perp)|^2\rangle & \text{if } \boldsymbol{k}_\perp \parallel \boldsymbol{e}_x \\ \langle|\tilde{n}_1(\boldsymbol{k}_\perp)|^2\rangle & \text{if } \boldsymbol{k}_\perp \parallel \boldsymbol{e}_y \end{cases} \qquad (4)$$

We can therefore conclude that even forward-scattering modes ($\boldsymbol{k}_\perp = \boldsymbol{0}$) can be observed with a good contrast in this setup. Furthermore, an eigenmode selection similar to the one in Giavazzi's setups happens along the x and y directions with a switch of $\tilde{n}_1$ and $\tilde{n}_2$, but this selection becomes broken (i.e. a mixture of eigenmodes contribute to scattering) when $\boldsymbol{k}_\perp$ has an arbitrary direction or when $|\boldsymbol{k}_\perp|$ is comparable to $k\sin 2\theta$. Assuming a mean wavelength of $0.6\,\mu$m, a mean refractive index of 1.6, and a tilt angle $\theta \approx 5^\circ$, this critical wavevector is found to be around $3\,\mathrm{rad}/\mu\mathrm{m}$, which is similar to the diffraction limit $k\mathrm{NA} \approx 4.2\,\mathrm{rad}/\mu\mathrm{m}$ and bigger than all wavevectors probed in the experiments presented in the following. I remark that in strongly chiral samples, the structure of fluctuation eigenmodes is more complicated than in nematics, and deviations from this ideal behaviour could happen because of cross-correlations between the directions x and y. These possible deviations will be discussed in Sec. 4.

To summarise this discussion, Giavazzi's setups for homeotropic samples are well-suited to study fluctuation modes with moderately large scattering wavevectors (up to the diffraction limit of the microscope), whereas the setup of Fig. 1a is better suited to the study of fluctuations with small scattering wavevectors. In this paper, only the latter setup is used.

2.3 Experimental validation in nematics

In Fig. 1c, I show snapshots of a typical acquisition done with a nematic sample of 5CB. The associated histogram of intensity values is shown in Fig. 1d. From this histogram, I calculate that 80 % of the intensity fluctuations δI deviate from the mean intensity I_{mean} by no more than $0.15 I_{\mathrm{mean}}$. This means that for the great majority of intensity fluctuations, the heterodyne scattering condition $\delta I \ll I_{\mathrm{mean}}$ is reasonably fulfilled and the DDM technique—which only works in the heterodyne regime[22]—can be applied to characterize the fluctuation modes. One may nevertheless wonder whether extreme fluctuations which do not fulfil the heterodyne condition could bias the DDM analysis. To assert this, let us compare measurements obtained from the setup of Fig. 1a with other measurements in the literature.

I recall that DDM is based on the measurement of an image stack $I(\boldsymbol{r}_\perp, t)$ (with $\boldsymbol{r}_\perp$ the pixel position and t the time) such as the one shown in Fig. 1c and the calculation of the so-called image structure function[22]:

$$D(\boldsymbol{k}_\perp, \Delta t) \equiv \left\langle \left[\tilde{I}(\boldsymbol{k}_\perp, t+\Delta t) - \tilde{I}(\boldsymbol{k}_\perp, t)\right]^2 \right\rangle_t, \qquad (5)$$

with $\tilde{I}$ the spatially Fourier-transformed acquisition stack, $\boldsymbol{k}_\perp$ the Fourier wavevector, and $\langle \ldots \rangle_t$ an ergodic average. I underline that the Fourier wavevector of the measured images is not parallel to the in-sample-plane xy associated with the scattering wavevectors, and in all rigour should be defined as the modified wavevector $\boldsymbol{k}'_\perp$ of the previous subsection, which is parallel to the $x'y'$ plane. However, since the tilt angle of the sample is around 5°, the difference between k_y and $k'_y \equiv k_y/\cos\theta$ is less than 0.15 % and can therefore be safely ignored.

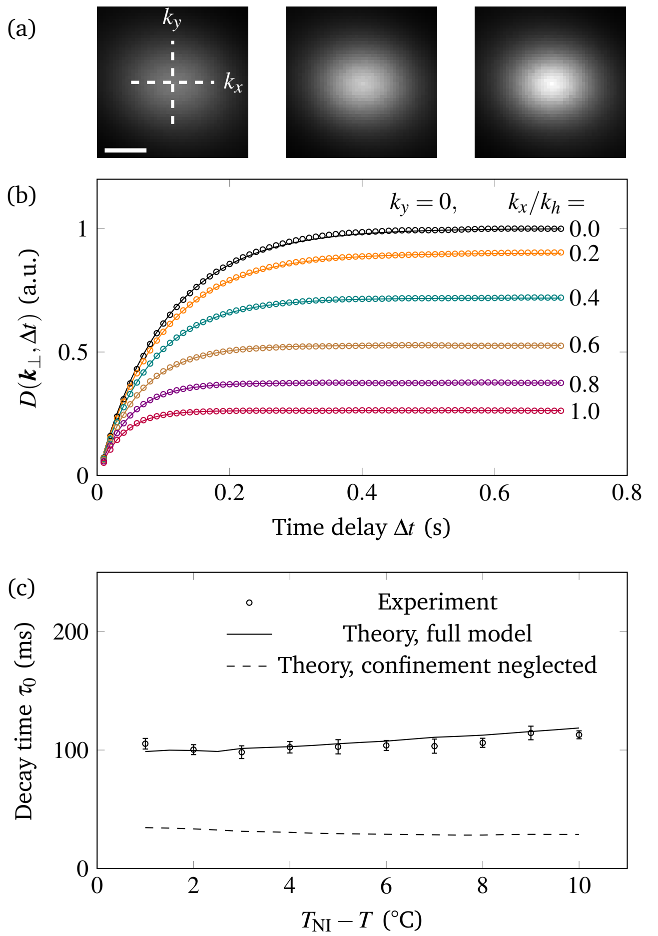

Fig. 2 (a) A few 2D image structure function, associated to $\Delta t = 5, 10, 15$ ms from left to right, as measured in a nematic sample of 5CB at $T_{\mathrm{NI}} - T = 5\,^\circ$C with a framerate of 100 Hz. The white bar represents a wavevector shift of $0.5\,\mathrm{rad}/\mu\mathrm{m}$, and the horizontal (resp., vertical) dashed line represents the k_x-axis (resp., k_y-axis) along which 1D temporal profiles of the image structure function are extracted. (b) 1D temporal profiles of the image structure function of (a) plotted against the time delay for a few transverse wavevectors. Experimental data correspond to markers, and the plain lines are the associated fit curves calculated with eqn (6). (c) Fundamental decay time $\tau_0 \equiv \tau(\boldsymbol{k}_\perp = \boldsymbol{0})$ as a function of temperature.

In the regime of validity of DDM, the image structure function can typically be fitted with the following one-decay-time law[22]:

$$D(\boldsymbol{k}_\perp, \Delta t) = A(\boldsymbol{k}_\perp)\left(1 - \exp\left[-\frac{\Delta t}{\tau(\boldsymbol{k}_\perp)}\right]\right) + B(\boldsymbol{k}_\perp) \qquad (6)$$

In the latter formula, $\tau(\boldsymbol{k}_\perp)$ is the decay time of the slowest fluctuation mode with transverse wavevector $\boldsymbol{k}_\perp$, $B(\boldsymbol{k}_\perp)$ is a non-thermal noise contribution, and $A(\boldsymbol{k}_\perp) \equiv M(\boldsymbol{k}_\perp)S(\boldsymbol{k}_\perp)$ is proportional to the scattering cross-section $S(\boldsymbol{k}_\perp)$ derived in the previous section. Following the formalism of Digital Fourier Microscopy introduced by Giavazzi *et al.* [26], the scattering cross-section $S(\boldsymbol{k}_\perp)$ will be identified with the static structure factor of the LC layer since both quantities are proportional to the correlation function of the fluctuating field (particle density in Giavazzi's case, director fluctuation in our case). Finally, $M(\boldsymbol{k}_\perp)$ can be interpreted as a setup-dependent factor related to the microscope, which may include a variety of effects such as spatial or temporal incoherence and finite sample thickness [27].

I underline that confined fluctuation modes are characterized by both the transverse wavevector $\boldsymbol{k}_\perp$ and the longitudinal wavevector k_z, which must be discretised since the sample thickness is finite [23]. However, as demonstrated experimentally and theoretically in a previous study with nematic samples [14], only the fundamental wavevector $k_z = k_h \equiv \pi/h$ significantly contributes to the image structure function since higher-order modes decay much faster. We will reach a similar conclusion for my cholesteric samples, which is why no k_z-dependence was introduced for the DDM quantities above.

For all studied samples, I systematically measured the image structure function after properly focusing the sample in the microscope, which can be done visually by minimizing the out-of-focus blur of the patterns visible in Fig. 1c. Since the numerical aperture of the objective and the sample tilt are small, this focusing can be achieved over the whole region of interest. The ergodic average in the definition of D is always done over 40000 images. A few 2D image structure function at fixed time delay Δt are shown in Fig. 2a, as measured in a nematic sample of 5CB with thickness $h \approx 11.6\mu$m. A few 1D temporal profiles of the image structure function of (a) with the associated fit using eqn (6) are shown in Fig. 2b. To reduce statistical noise, these 1D profiles were averaged over a 3x3 region centred on each wavevector. As visible, the experimental data is well-fitted by the one-decay-time law, which further justifies our choice to ignore the dependence of DDM quantities on k_z. However, I note that the 3x3 averaging may bias the fitted relaxation time since τ typically varies quadratically in $\boldsymbol{k}_\perp$. For this reason, a different and non-biased averaging method was used to extract the relaxation time $\tau(\boldsymbol{k}_\perp)$ from all the measured DDM stacks in this paper.

In principle, the bow-tie-shape azimuthal averaging method of Ref. [22] is well-suited to the task. Indeed, the latter method is non-biased since the average is done over a limited azimuthal range where the DDM signal is almost constant, but the calculation of uncertainties is unfortunately not detailed in Ref. [22]. For this reason, I used a slightly different approach based on surface fitting instead of azimuthal averaging. The first step of this new approach is to fit the raw DDM data with eqn (6) for every discretized wavevector $\boldsymbol{k}_\perp$, without any averaging of the DDM signal. The resultant fitted decay times will be denoted as $\tau_{\text{noisy}}(\boldsymbol{k}_\perp)$ since they were obtained from noisy DDM signals. The second step is to locally fit $\tau_{\text{noisy}}(\boldsymbol{k}_\perp)$ with a quadratic polynomial surface inside a 5-pixel-wide square region centred on any target wavevector $\boldsymbol{k}_{\perp 0}$, and deduce the value of $\tau(\boldsymbol{k}_{\perp 0})$ from the centre value of the fitted surface. Finally, the uncertainty of $\tau(\boldsymbol{k}_{\perp 0})$ can be estimated as $3\sqrt{C}$, with C the diagonal entry of the surface fit covariance matrix associated with $\tau(\boldsymbol{k}_{\perp 0})$.

Table 1 Elastic constants (in pN) and viscosities (in mPa.s) of 5CB at $T_{\text{NI}} - T = 5\,^\circ$C measured by Cui and Kelly [11].

K_1	K_2	K_3	γ_1	η_a	η_b	η_c	η_{bc}
4.81	2.80	6.26	56	33.2	17.7	73.8	45.8

On Fig. 2c, the fundamental decay time $\tau_0 \equiv \tau(\boldsymbol{k}_\perp = \boldsymbol{0})$ is plotted against $T_{\text{NI}} - T$, with T the temperature and T_{NI} the nematic/isotropic transition temperature, which is systematically measured for each sample and is typically around $35.5\,^\circ$C. To validate these measurements, let us estimate their theoretical values using the values of the material constants of 5CB measured by Cui and Kelly [11] with a dynamical light scattering setup. For this study, the relevant material constants are the Frank elastic constants K_1, K_2 and K_3 respectively associated with splay, twist and bend deformations, as well as the rotational viscosity γ_1, the Miesowicz viscosities η_a, η_b, and η_c, and an additional viscosity η_{bc} that will be used later in this paper but is unimportant for now. The definition of these viscosities in terms of the Leslie viscosities α_j $(j = 1\ldots6)$ will be given in Sec. 3.1.

Čopič *et al.* theoretically calculated the decay time of the fundamental fluctuation mode in a homeotropic nematic sample at $\boldsymbol{k}_\perp = \boldsymbol{0}$ and found [14]:

$$\tau_0 = \frac{\gamma_1(1-\mu)}{K_3\phi_\tau^2}\left(\frac{2}{h}\right)^2, \tag{7}$$

where the parameter ϕ_τ can be found as the solution of:

$$\cos\phi_\tau = \mu\,\mathrm{sinc}\,\phi_\tau. \tag{8}$$

In these equations, μ is a parameter which sets the strength of the coupling between hydrodynamics and director relaxation and is defined as:

$$\mu \equiv \frac{\alpha_2^2}{\gamma_1\eta_c} = \frac{(\eta_b - \eta_c - \gamma_1)^2}{4\gamma_1\eta_c}, \tag{9}$$

where the last equality can be deduced from the viscosity definitions in Sec. 3.1. Table 1 includes the value of the material constants at $T - T_{\text{NI}} = 5\,^\circ$C, and the values at other temperatures can be obtained from Ref. [11]. Using those, I plotted eqn (7) against the temperature as a plain line in Fig. 2c without adjusting any parameter. One can observe an excellent agreement with our DDM measurements with an average deviation less than 3.6 %, which demonstrates the validity of the novel DDM geometry presented here.

Interestingly, one may notice that the decay time τ_0 is almost independent of the temperature in 5CB, which is due to the very similar temperature dependence of γ_1 and K_3 and an almost T-independent μ parameter. Furthermore, the originality of Čopič formula in eqn (7) is to introduce a correction term due to the interaction between the sample boundaries and the hydrodynamic flow created by the relaxing fluctuation mode. When this interaction is neglected, one obtains the same formula with $\phi_\tau = \pi/2$ (which is a solution of eqn (8) only if $\mu = 0$, which is not true in general), leading to an inferior agreement with the experiment as demonstrated by the plotted dash line in Fig. 2c. This further demonstrates the delicate coupling between hydrodynamics, confinement and thermal fluctuations in light scattering experiments with liquid crystals.

2.4 Critical behaviour in unwound cholesterics

Let us now consider measurements with cholesteric samples. Since different samples may be associated with slightly different thicknesses, one needs to be very careful when comparing measurements between different samples. In short, we must properly scale measured quantities to be able to compare them between different samples. To find the relevant scaling, let us apply dimensional analysis to our system considering only the fundamental relaxation time τ_0. Inspired by the model of Čopič *et al.*[14], we know that τ_0 will depend on γ_1, μ, K_3 and h. But in a cholesteric, it must also depend on the spontaneous twist q and the twist elastic constant K_2, since deformations of the equilibrium unwound state are twisted in a chiral sample. We then have a relation between 7 parameters with 3 physical dimensions (time, length and mass). According to the Buckingham π theorem, we can reduce this relation to another one between 4 dimensionless parameters. This relation can be conveniently expressed in terms of a universal function f:

$$\frac{\tau_0}{\tau_h} = f\left(\frac{q}{q_c}, \mu, \frac{K_2}{K_3}\right), \tag{10}$$

with $\tau_h \equiv \gamma_1(1-\mu)/(K_3 k_h^2)$, $q_c \equiv (K_3/K_2)k_h$ and $k_h \equiv \pi/h$. I emphasize that q_c corresponds to the (positive) critical spontaneous twist at which a right-handed unwound cholesteric destabilizes[19*]. In addition, Eq. 10 must be invariant under the mirror symmetry because the decay time should be the same in a left-handed and right-handed cholesteric. This means that f is an even function of q/q_c, since q—a pseudo-scalar—is the only quantity that changes sign under the mirror transformation.

In the experiments, the spontaneous twist q is varied by changing the mass fraction C of R811, which are linked together through the definition of the helical twist power $\mathrm{HTP} = q/(2\pi C)$. Since the mass fractions of R811 are rather small, one can assume that the HTP, elastic constants and viscosities are all independent of C. One can therefore define a critical mass fraction $C_c \equiv q_c/(2\pi\,\mathrm{HTP})$ such that $q/q_c = C/C_c$, and conclude that the relation between τ/τ_h and C/C_c should be described by a universal even function in our experiments.

To test this, I prepared 12 samples with mass fractions of R811 between 0 and 0.719 wt% and thicknesses between 10 and 12 μm and measured for each sample the image structure function and decay frequencies using the procedure described above. Some samples with inhomogeneous thickness allowed multiple measurements in different parts of the sample, thanks to the careful thickness cartography established before filling any sample as explained above. All measurements were done at $T - T_{\mathrm{NI}} = 5\,^\circ$C. Each measurement is associated with a unique thickness value that allows the calculation of τ_h and C_c using their definitions and the material constant values in Table 1. When the rescaled mass fraction of chiral molecules C/C_c is above 0.8, the density of localized and metastable topological solitons perturbing the homeotropic unwound state (such as cholesteric fingers and bubbles[19]) becomes too high. These localized director perturbations prevent the DDM technique to be applied since they break the translational invariance. In principle, this range of mass fractions could be slightly extended up to a higher mass fraction $C_c' < C_c$ (with $C_c' > 0.8C_c$) at which the line tension of cholesteric fingers becomes zero[19]. Indeed, below C_c', isolated cholesteric fingers with positive line tensions trapped between dust particles could be erased by using ITO-covered glass plates and applying an electric field. However, between C_c' and C_c, cholesteric fingers have a negative line tension and will therefore grow again in the absence of an electric field, thereby preventing their elimination. Since it is sufficient for our goal, I focus here on samples without ITO electrodes and with $C < 0.8C_c$, for which one can always find a homeotropic region with a typical extent of 200 μm.

Fig. 3a shows a few 1D temporal profiles of the image structure function at $\boldsymbol{k}_\perp = \boldsymbol{0}$ for different rescaled mass fraction of R811 C/C_c. From this plot, we deduce that the fundamental relaxation time $\tau_0 \equiv \tau(\boldsymbol{k}_\perp = \boldsymbol{0})$ seem to increase with C/C_c. To better quantify this variation, Fig. 3b shows the fundamental rescaled decay frequency τ_h/τ_0 as a function of C/C_c. As visible, all experimental data collapse on the same master curve, in full agreement with the dimensional analysis above. Furthermore, one observes that the decay frequency is greatly reduced as C increases, and seems to even go to 0 as C approaches the critical mass fraction C_c. This critical behaviour should come as no surprise for the reader since phase transitions are generally associated with a critical slowing down of a few fluctuation modes—the so-called *soft modes* of the transition. In our case, the transition is not a phase transition in the thermodynamic sense but rather a structural transition corresponding to the elastic destabilization of the unwound state at $C = C_c$. More quantitatively, the experimental data of Fig. 3b is well-fitted with the following even function (shown with a plain line in Fig. 3b):

$$\frac{\tau_h}{\tau_0} = \frac{1 - (C/C_c)^2}{T_0 - T_1\,(C/C_c)^2}, \tag{11}$$

with $T_0 = 3.52 \pm 0.12$ and $T_1 = 0.40 \pm 0.3$ two coefficients which only depends on μ and K_2/K_3 according to the dimensional analysis above. The numerator in eqn (11) is directly associated with the vanishing of the fundamental decay frequency at $C = C_c$ and is compatible with the experimentally-observed horizontal slope at $C = 0$, whereas the denominator corresponds to correction terms associated with the coupling between hydrodynamics and director relaxation. This law will be justified in more detail in Sec. 3 and discussed in Sec. 4. Here, I will only emphasize that the critical behaviour is mainly determined by the numerator of eqn (11), which has no adjustable parameter. We can therefore conclude that our measurement of the HTP with Cano wedge samples (which sets the amplitude of the critical mass fraction C_c) is fully compatible with the critical slowing down of the fluctuations observed with DDM.

In addition to the fundamental fluctuation mode at $\boldsymbol{k}_\perp = \boldsymbol{0}$,

---

[*] Conversely, a left-handed unwound cholesteric destabilizes when $q = -q_c$.

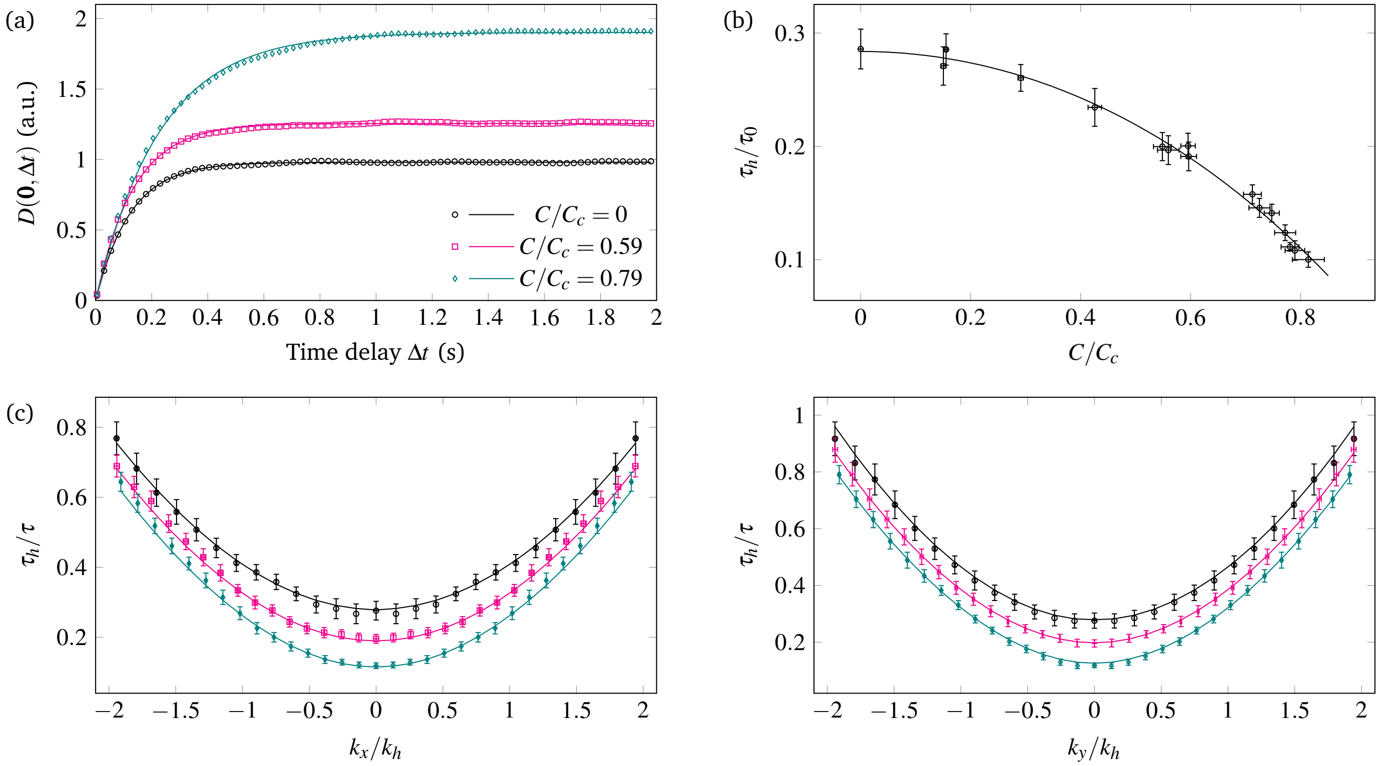

Fig. 3 (a) 1D temporal profiles of the image structure function at $\boldsymbol{k}_\perp = \mathbf{0}$, plotted against the time delay for three different rescaled mass fractions of chiral molecules C/C_c. (b) Rescaled fundamental decay frequency τ_h/τ_0 as a function of C/C_c. (c) Dispersion curve of decay frequencies as a function of the rescaled wavevector k_x/k_h (left) and k_y/k_h (right) for three different C/C_c. The legend in (a) also applies to (c). For all plots, markers correspond to experimental data and plain lines correspond to fit data. All experimental data associated with (a,c) (resp., (b)) were obtained with a framerate of 200 Hz (resp., 100 Hz). The fit lines in (a) (resp., (b)) were calculated with eqn (6) (resp., eqn (11)). The fit lines in (c) were obtained from the theoretical model introduced in Sec. 3 and discussed in Sec. 4.

the DDM approach also gives the decay frequencies when $\boldsymbol{k}_\perp \neq \mathbf{0}$. Fig. 3c shows a few dispersion curves (τ_h/τ plotted against $|\boldsymbol{k}_\perp|/k_h$) when the wavevector $\boldsymbol{k}_\perp$ is along x or y, restricting the analysis to wavevectors of amplitude less than 0.6 rad/μm and taking into account the selection rule of fluctuation eigenmodes described in Sec. 2.2. In this figure, one may observe that the modes selected when $\boldsymbol{k}_\perp$ is along y decay faster than the ones with $\boldsymbol{k}_\perp$ along x, which indicates that there exist two branches of fluctuations modes with different dissipations. This experimental result will be discussed in more depth in Sec. 3 and 4, where we will explain how these dispersion curves can be reasonably fitted (plain lines in Fig. 3c) with a full model of fluctuation modes in unwound cholesterics. In addition, an attentive reader will notice that the decay frequencies decrease with the mass fraction C of R811 whatever the value of the wavevector $\boldsymbol{k}_\perp$, showing that chirality affects the dynamics of all fluctuation modes, not simply the fundamental one. However, I emphasize that only the mode at $\boldsymbol{k}_\perp = \mathbf{0}$ is associated with a critical divergence of the decay time, and therefore only this fundamental mode can be considered as the soft mode driving the destabilization of the unwound state.

Up until now, we have focused on the dynamical properties of the fluctuation modes, i.e. their decay frequencies. Let us now examine their static properties by trying to estimate the static structure factor $S(\boldsymbol{k}_\perp)$ from the image structure function. As explained before, the coefficient $A(\boldsymbol{k}_\perp)$ in eqn (6) is equal to $M(\boldsymbol{k}_\perp)S(\boldsymbol{k}_\perp)$, with M a function depending on the optical details of the microscope setup. The function M was characterized in depth by Giavazzi *et al.* for a depolarized DDM setup optimized for the study of colloidal suspensions, taking into account finite-size effects and partial temporal and spatial coherence of the illumination setup. Their calculation showed that for large wavevectors, the function M is not constant and one cannot estimate directly the static structure factor from $A(\boldsymbol{k}_\perp)$ (at least not without using the theoretical expression of $M(\boldsymbol{k}_\perp)$); conversely, for small wavevectors, the Taylor expansion of $M(\boldsymbol{k}_\perp)$ up to order 1 is independent of $\boldsymbol{k}_\perp$ (no linear dependence in $\boldsymbol{k}_\perp$) and M can be considered as a non-essential multiplicative factor. Generalizing these results to the polarized DDM setup used here is outside the scope of this paper, so let us instead focus on the regime of small wavevectors, in which we can reasonably assume that the function M is also constant.

According to a calculation by Zel'dovich and Tabiryan[23], the fundamental fluctuation mode of a confined nematic sample is associated with a Lorentzian contribution to the static structure factor. Assuming that this statement stays true in a cholesteric and that higher-order modes do not significantly contribute to the structure factor, we can take $S(\boldsymbol{k}_\perp)$ under the following form

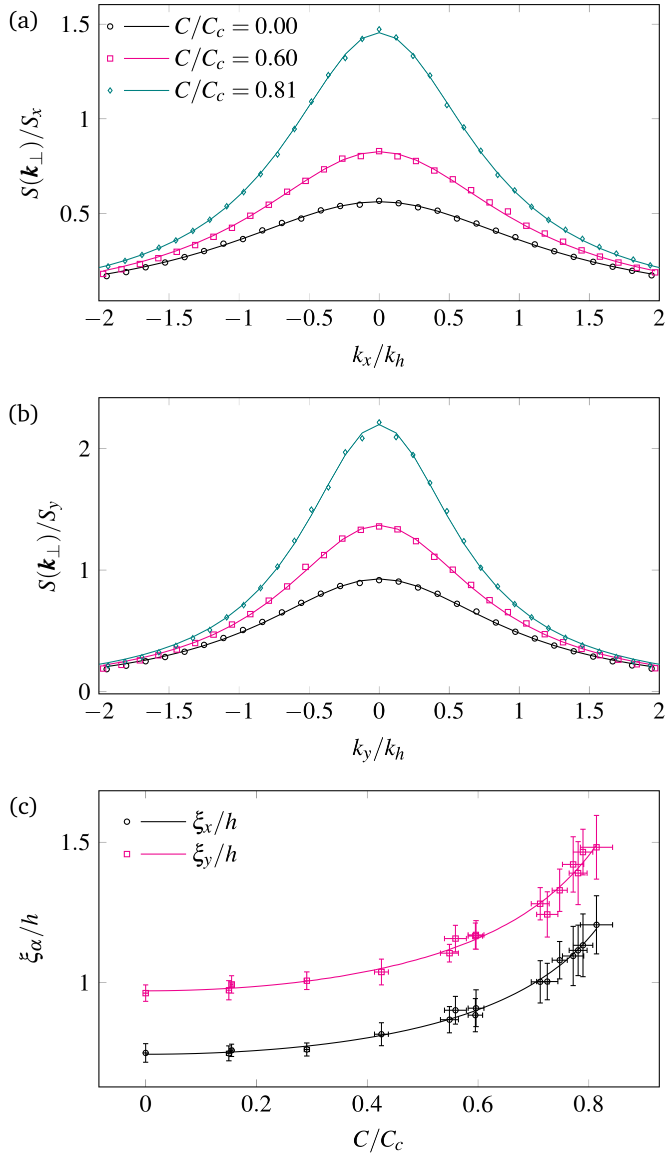

Fig. 4 (a,b) Rescaled static structure factor as a function of the rescaled wavevector when $\boldsymbol{k}_\perp$ is parallel to x (a) or y (b), for three different mass fractions of R811. The legend in (a) also applies to (b). (c) Rescaled correlation lengths plotted against the rescaled mass fraction of chiral molecules. In (a,b,c), markers (plain lines) correspond to experimental data obtained with a framerate of 100 Hz (theoretical fits using eqn (12) for a–b and eqn (13) for c).

for our setup:

$$S(\boldsymbol{k}_\perp) = \begin{cases} S_x\left[\left(\frac{h}{\xi_x}\right)^2 + \left(\frac{k_x}{k_h}\right)^2\right]^{-1} & \text{if } \boldsymbol{k}_\perp \parallel \boldsymbol{e}_x \\ S_y\left[\left(\frac{h}{\xi_y}\right)^2 + \left(\frac{k_y}{k_h}\right)^2\right]^{-1} & \text{if } \boldsymbol{k}_\perp \parallel \boldsymbol{e}_y \end{cases} \tag{12}$$

with S_α a constant and ξ_α the correlation length along the direction $\alpha = x$ or y, using again the fact that different types of fluctuation modes are selected along the x and y directions. Since we assumed that M is a constant for small wavevectors, the function $A(\boldsymbol{k}_\perp)$ can also be fitted by the same law with a coefficient A_α instead of S_α, and data from different samples can be compared by plotting $A/A_\alpha = S/S_\alpha$ against k_α/k_h ($\alpha = x, y$), as shown in Fig. 4a–b. From this graph, one can conclude that eqn (12) fits very well the experimental data when $|\boldsymbol{k}_\perp|$ is less than $0.6\,\mathrm{rad}/\mu\mathrm{m}$, which is approximately 8 times smaller than the diffraction limit of our microscope objective. For wavevectors of higher amplitude, I found out that the measured $A(\boldsymbol{k}_\perp)$ decay exponentially instead of algebraically, which could likely be explained by an accurate modelling of the microscope function $M(\boldsymbol{k}_\perp)$.

From the theoretical fits of the static structure factor for each sample, one obtains the rescaled correlation lengths ξ_x/h and ξ_y/h as a function of the rescaled mass fraction of R811 C/C_c, as plotted in Fig. 4c. Similar to the critical divergence of the decay time, one may observe that the correlation lengths also seem to diverge when $C \to C_c$. More quantitatively, the experimental curves in Fig. 4c are well-fitted with the following law ($\alpha = x$ or y):

$$\frac{\xi_\alpha}{h} = \frac{G_\alpha}{\left[1-(C/C_c)^2\right]^\nu}, \tag{13}$$

with $\nu \approx 0.4$. I underline that the shape of $M(\boldsymbol{k}_\perp)$ could bias the estimation of the correlation lengths from our experimental data. However, this bias should be the same whatever the mass fraction of chiral molecules and will therefore not change the observed critical behaviour.

Summarizing the experimental results of this section, I showed that criticality can be found in the dynamic and static properties of the fluctuation modes, with a divergence of the decay times and correlation lengths when $C \to C_c$. To better characterize these critical behaviours, the next two sections will introduce and discuss a complete model of the decay dynamic of fluctuation modes in unwound cholesteric.

3 Theoretical model of confined chiral fluctuations

3.1 Relaxation dynamics

The main goal of this section is to theoretically calculate the relaxation times and director/velocity profiles associated with the fluctuation modes of an unwound cholesteric sample with homeotropic alignment. All calculations are done in the referential of the sample $(\boldsymbol{e}_x, \boldsymbol{e}_y, \boldsymbol{e}_z)$ as defined in Fig. 1a, with the z-coordinate varying from $-h/2$ to $h/2$. The director field is written as $\boldsymbol{n} = \sqrt{1-|\boldsymbol{n}_\perp|^2}\boldsymbol{e}_z + \boldsymbol{n}_\perp$, with $\boldsymbol{n}_\perp \perp \boldsymbol{e}_z$ the fluctuating part. The hydrodynamic velocity $\boldsymbol{v}$ is also decomposed into its transverse part $\boldsymbol{v}_\perp$ and longitudinal part $v_z\boldsymbol{e}_z$. By linearising the equations of nematodynamics[19] around the equilibrium state $\boldsymbol{n} = \boldsymbol{e}_z$ and $\boldsymbol{v} = \boldsymbol{0}$, the linearised torque equation is found to be:

$$\begin{aligned} \gamma_1\partial_t\boldsymbol{n}_\perp + \alpha_2\partial_z\boldsymbol{v}_\perp + \alpha_3\boldsymbol{\nabla}_\perp v_z = \left(K_2\Delta_\perp + K_3\partial_z^2\right)\boldsymbol{n}_\perp \\ + (K_1-K_2)\,\boldsymbol{\nabla}_\perp\boldsymbol{\nabla}\cdot\boldsymbol{n}_\perp - 2K_2q\boldsymbol{e}_z\times\partial_z\boldsymbol{n}_\perp. \end{aligned} \tag{14}$$

The coupling with hydrodynamics is taken into account with the Leslie viscosities α_2 and α_3, $\gamma_1 \equiv \alpha_3 - \alpha_2$ is the rotational viscosity, q is the spontaneous twist of the cholesteric and $K_{1,2,3}$ are the splay, twist and bend elastic constants. The velocity field $\boldsymbol{v}$ can be calculated from the linearised momentum equation (i.e. the Stokes equation) $\rho\partial_t\boldsymbol{v} = \boldsymbol{\nabla}\cdot\boldsymbol{\sigma}$ and incompressibility condition $\boldsymbol{\nabla}\cdot\boldsymbol{v} = 0$, with ρ the fluid density and $\boldsymbol{\sigma}$ the stress tensor.

By linearising the general expression of the stress tensor of a nematic/cholesteric LC[19], I find that the Stokes equation can be rewritten as follows:

$$\rho\partial_t \boldsymbol{v}_\perp + \boldsymbol{\nabla}_\perp P = \alpha_2\partial_z\partial_t\boldsymbol{n}_\perp + \left[\eta_a\Delta_\perp + \eta_c\partial_z^2\right]\boldsymbol{v}_\perp, \tag{15}$$

$$\rho\partial_t v_z + \partial_z P = \alpha_3\boldsymbol{\nabla}\cdot\partial_t\boldsymbol{n}_\perp + \left[\eta_b\Delta_\perp + (2\eta_{bc}-\eta_a)\,\partial_z^2\right]v_z, \tag{16}$$

where $\eta_a \equiv \alpha_4/2$, $\eta_b \equiv (\alpha_3+\alpha_4+\alpha_6)/2$ and $\eta_c \equiv (\alpha_5+\alpha_4-\alpha_2)/2$ are the usual Miesowicz viscosities defined as functions of the Leslie viscosities α_{1-6} and $\eta_{bc} = (\alpha_1+\eta_b+\eta_c)/2$ is an additional viscosity relevant to the relaxation of splay-bend modes[14]. These equations are given in an especially compact form thanks to the Parodi relation[19] $\alpha_2+\alpha_3 = \alpha_6-\alpha_5$, the incompressibility identity $\partial_z v_z = -\boldsymbol{\nabla}\cdot\boldsymbol{v}_\perp$ and a redefinition of the pressure $P \to P-(\alpha_2+\alpha_5)\partial_z v_z/2$—which is allowed since pressure is a Lagrange multiplier in the limit of perfect incompressibility. They can be checked to agree with other (usually longer) forms given in the literature[14,28]. I assume that there is no hydrodynamic slip on the confining boundaries (i.e. zero-Dirichlet boundary conditions for $\boldsymbol{v}$). Using the incompressibility condition, these boundary conditions (BCs) also imply $\partial_z v_z = 0$ on the confining plates (i.e. zero-Neumann BCs for v_z). I also recall that thermodynamic stability imposes the following inequalities for the viscosities[19]:

$$\gamma_1 > 0, \quad \eta_a > 0, \quad \eta_b > \frac{\alpha_3^2}{\gamma_1}, \quad \eta_c > \frac{\alpha_2^2}{\gamma_1}, \quad \eta_{bc} > \frac{\alpha_2+\alpha_5}{2} \tag{17}$$

The next step is to eliminate the pressure from eqn (15,16) and neglect the inertia terms since the associated relaxation time $\tau_i \equiv \rho l^2/\eta_a$ (with l a typical length comprised between the thickness h and the region-of-interest width L) can be estimated to be smaller than $3\,\mu$s, which is much smaller than all relaxation times considered in this paper. I then find an analytical solution for the velocity components, expressed in terms of the time-derivative of the director field:

$$\boldsymbol{e}_z\cdot\boldsymbol{\nabla}\times\boldsymbol{v}_\perp = -\left[\mathscr{H}^{\mathrm{TB}}\right]_{\mathrm{D}}^{-1}\mathscr{C}^{\mathrm{TB}}\partial_t\left(\boldsymbol{e}_z\cdot\boldsymbol{\nabla}\times\boldsymbol{n}_\perp\right), \tag{18}$$

$$v_z = -\left[\mathscr{H}^{\mathrm{SB}}\right]_{\mathrm{D,N}}^{-1}\mathscr{C}^{\mathrm{SB}}\partial_t\left(\boldsymbol{\nabla}\cdot\boldsymbol{n}_\perp\right), \tag{19}$$

with the following differential operator definitions:

$$\mathscr{H}^{\mathrm{TB}} = \eta_a\Delta_\perp + \eta_c\partial_z^2, \quad \mathscr{H}^{\mathrm{SB}} = \eta_b\Delta_\perp^2 + 2\eta_{bc}\partial_z^2\Delta_\perp + \eta_c\partial_z^4, \tag{20}$$

$$\mathscr{C}^{\mathrm{TB}} = \alpha_2\partial_z, \qquad \mathscr{C}^{\mathrm{SB}} = \alpha_3\Delta_\perp - \alpha_2\partial_z^2. \tag{21}$$

Eqn (18,19) rely on a compact notation for the inverse of any differential operator $\mathscr{D}$, where calculating $v = [\mathscr{D}]_{\mathrm{D}}^{-1}u$ (resp., $v = [\mathscr{D}]_{\mathrm{D,N}}^{-1}u$) means solving the differential equation $\mathscr{D}v = u$ with zero-Dirichlet boundary conditions (resp., zero-Dirichlet and zero-Neumann boundary conditions). This notation is particularly convenient and clear when numerically discretising the problem on a mesh since in this case any differential operator (resp., function) is transformed into a sparse matrix (resp., vector). In this discrete setting, calculating $v = [\mathscr{D}]^{-1}u$ is equivalent to calculating the matrix-vector product with the matrix inverse $[\mathscr{D}]^{-1}$, which can be easily done (again with appropriate BCs) using conventional tools of linear algebra.

In Eqn (18,19), the director field is naturally split into two independent contributions associated with splay-bend (SB) deformations ($\boldsymbol{\nabla}\cdot\boldsymbol{n}_\perp \neq 0$) or twist-bend (TB) deformations ($\boldsymbol{e}_z\cdot\boldsymbol{\nabla}\times\boldsymbol{n}_\perp \neq 0$). This split is similar to the Helmholtz decomposition of hydrodynamics since these contributions are respectively associated with curl-free and divergence-free vector fields. From a physical point of view, eqn (18) (resp., (19)) shows that the relaxation of a twist-bend (resp., splay-bend) director deformation will induce a hydrodynamic flow in the plane (resp., out of the plane) of the sample. The shapes of these flows for fundamental splay-bend or twist-bend deformations are schematized in Fig. 5. These hydrodynamic flows will in turn modify the torque equation (14) and lower the effective dissipation by helping the director to relax towards equilibrium, leading to the so-called backflow effect of LCs. To better see this, eqn (18,19) can be used to fully eliminate the velocity from the torque equation (14):

$$\left[\boldsymbol{\Gamma}\partial_t + \mathbf{L}\right]\begin{pmatrix}\boldsymbol{\nabla}\cdot\boldsymbol{n}_\perp \\ \boldsymbol{e}_z\cdot\boldsymbol{\nabla}\times\boldsymbol{n}_\perp\end{pmatrix} = 0, \tag{22}$$

In the latter equation, $\boldsymbol{\Gamma}$ is a differential operator representing the effective rotational dissipation and $\mathbf{L}$ is a differential operator governing the elastic response of the LC:

$$\boldsymbol{\Gamma} \equiv \begin{pmatrix}\Gamma^{\mathrm{SB}} & 0 \\ 0 & \Gamma^{\mathrm{TB}}\end{pmatrix}, \quad \mathbf{L} \equiv \begin{pmatrix}-K_1\Delta_\perp - K_3\partial_z^2 & -2K_2 q\partial_z \\ 2K_2 q\partial_z & -K_2\Delta_\perp - K_3\partial_z^2\end{pmatrix}, \tag{23}$$

$$\Gamma^{\mathrm{SB}} \equiv \gamma_1 - \mathscr{C}^{\mathrm{SB}}\left[\mathscr{H}^{\mathrm{SB}}\right]_{\mathrm{D,N}}^{-1}\mathscr{C}^{\mathrm{SB}}, \tag{24}$$

$$\Gamma^{\mathrm{TB}} \equiv \gamma_1 - \mathscr{C}^{\mathrm{TB}}\left[\mathscr{H}^{\mathrm{TB}}\right]_{\mathrm{D}}^{-1}\mathscr{C}^{\mathrm{TB}}. \tag{25}$$

Eqn (22) is the general differential equation governing the relaxation of a weakly deformed director field with backflow. To the best of my knowledge, backflow effects were never derived under this specific general form and instead are usually characterized by fully solving the coupled torque and hydrodynamic equation for a specific system and defining at the end of the calculation an effective rotational viscosity $\gamma_1^\star$ lower than γ_1[14,19,28,29]. The formalism adopted here has many advantages. First, it explicitly shows that SB and TB modes have generally different dissipation due to the backflow contributions, which must be smaller than γ_1 since the operators after the minus signs in eqn (24,25) are self-adjoint positive operators[†]. Second, it can be applied for any geometry with weakly deformed directors, beyond the homeotropic sample studied here, on condition that appropriate BCs are used for the considered geometry. For example, a planar sample would correspond to confining plates normal to the x or y directions instead of z, with the director still aligned along z. Third, it takes into account the spontaneous twist of a cholesteric, which couples together SB and TB modes because of the symmetry breaking.

[†] The positive-definiteness of these operators can be deduced from a Fourier decomposition and the thermodynamic inequalities of eqn 17.

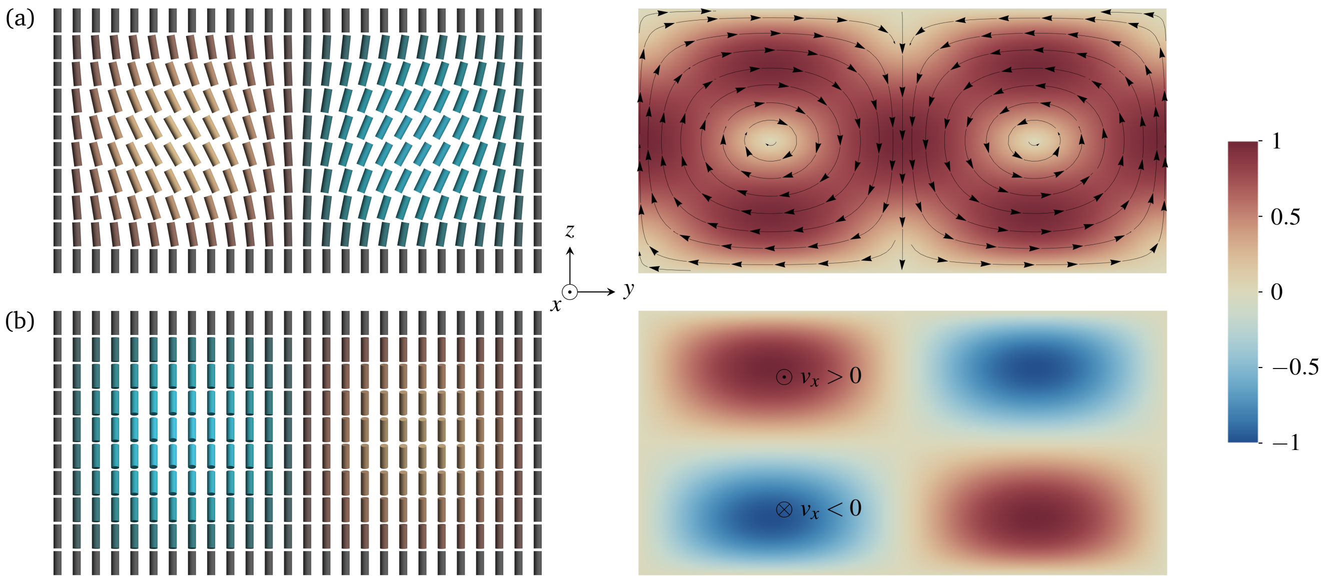

Fig. 5 (a) Schematics of a fundamental splay-bend director deformation (left) and the associated hydrodynamic flow (right) when the LC relax to equilibrium. (b) Same as (a) for a fundamental twist-bend deformation. The colour scale is common to both right images and corresponds to the normalized amplitude of $\sqrt{v_y^2+v_z^2}$ for (a) and v_x for (b). The hydrodynamic flow was calculated using the material constants of Table 1.

Fourth, for an unconfined nematic sample ($q=0$), one immediately finds that the dissipation operators in eqn (24,25) calculated in Fourier space exactly corresponds to the effective rotational dissipation of bulk SB and TB modes (see for example eqn (1) in Ref.[14]). Finally, and as already noted above, eqn (22) can be easily numerically discretised using a combination of sparse matrices, and allows to immediately obtain a director field solution without having to explicitly calculate the hydrodynamic velocity.

3.2 Eigenmodes of thermal fluctuations

3.2.1 Eigenvalue system

Let us now switch to the calculation of the fluctuation modes induced by thermal noise. Following the approach of Čopič *et al.*[14], I calculate those from the eigenvalues and eigenmodes of eqn (22), assuming exponentially-decaying modes. But before this, let us make an important point concerning the amplitude of fluctuation modes, which must be calculated from the thermodynamic equipartition theorem following the methodology of Zel'dovich *et al.*[23]. In this calculation, the amplitude of any eigenmode of the elasticity operator $\mathbf{L}$ with eigenvalue Λ is found to be proportional to k_BT/Λ. The problem here is that the dynamically-decaying eigenmode profiles of eqn (22) are not the same as the eigenmode profiles of $\mathbf{L}$ due to the inclusion of confined backflow—a dissipative phenomenon not related to the equilibrium equipartition theorem. In short, it is not really clear at first sight how the eigenmode amplitudes in the former equation should be linked to the eigenmode amplitudes calculated from equipartition.

This problem can be solved by observing that the backflow associated with a relaxing director eigenmode of eqn (22) needs a finite time to reach a stationary regime, which is set by the hydrodynamic relaxation time τ_i associated with inertia in eqn (15,16). To better illustrate this, let us consider a fluid initially at rest and a random thermal event which generates at $t=0$ an initial director field equal to one of the eigenmodes of $\mathbf{L}$. At time scales $t<\tau_i$, the velocity field grows from 0 and starts perturbing this initially pure eigenmode, while at times $t\gg\tau_i$, the director field is decomposed into a sum of eigenmodes of eqn (22) which exponentially decay with time. In short, eqn (22) is only valid at times longer than the relaxation time of the hydrodynamic velocity and cannot make the link between the short-time regime (equipartition theorem) and long-time regime (eigenmode relaxation with backflow). In principle, only the original eqn (14,15,16) allows the numerical calculation of this complicated eigenmode transformation process, which should be done starting from a null velocity and an eigenmode profile of $\mathbf{L}$ calculated from the equipartition theorem for the director. However, the hydrodynamic relaxation time τ_i cannot be probed in my experiments since it is too small, so let us ignore this difficult calculation of the mode amplitudes and focus instead on the relaxation time and profiles of the fluctuation modes in the long-time regime.

Since the LC layers in the experiments are ~ 2000 wider than they are thick, let us assume that the fluctuation modes are confined only in the z-direction and search eigenmodes using Fourier modes in the plane of the sample:

$$\boldsymbol{n}_\perp(\boldsymbol{r}_\perp,z,t)=\tilde{\boldsymbol{n}}_\perp(\boldsymbol{k}_\perp,z)\exp\left[i\boldsymbol{k}_\perp\cdot\boldsymbol{r}_\perp-t/\tau\right], \tag{26}$$

with τ the decay time and $\boldsymbol{k}_\perp$ the in-sample-plane wavevector of the eigenmode. Using eqn (22), I find that the eigenmode profile $\tilde{\boldsymbol{n}}_\perp(\boldsymbol{k}_\perp,z)\equiv\tilde{n}^{\mathrm{SB}}(\boldsymbol{k}_\perp,z)\boldsymbol{e}_k+\tilde{n}^{\mathrm{TB}}(\boldsymbol{k}_\perp,z)\boldsymbol{e}_z\times\boldsymbol{e}_k$ (with $\boldsymbol{e}_k=\boldsymbol{k}_\perp/|\boldsymbol{k}_\perp|$) and eigenvalue $f\equiv 1/\tau$ must be calculated from the following generalized eigenvalue problem:

$$\left[\tilde{\mathbf{L}} - f\tilde{\boldsymbol{\Gamma}}\right]\begin{pmatrix}\tilde{n}^{\mathrm{SB}}\\ \tilde{n}^{\mathrm{TB}}\end{pmatrix} = \mathbf{0}, \tag{27}$$

where $\tilde{\mathbf{L}}$ (resp., $\tilde{\boldsymbol{\Gamma}}$) is obtained from the in-sample-plane Fourier transform of $\mathbf{L}$ (resp., $\boldsymbol{\Gamma}$), i.e. making the substitution $-\Delta_\perp \to |\boldsymbol{k}_\perp|^2$.

3.2.2 Dispersion relation for small transverse wavevectors

Let us first focus on the small wavevector limit $|\boldsymbol{k}_\perp| \to 0$. Under this limit, the actions of the dissipation operators have relatively simple analytic expressions which are given in the ESI†, and I find that eqn (27) can be transformed into a simpler eigenvalue problem by introducing the rescaled coordinate $Z \equiv 2z/h$ and the modified eigenmode profiles $m^{\mathrm{SB}}(Z)$ and $m^{\mathrm{TB}}(Z)$ as follows:

$$\tilde{n}^{\mathrm{SB}}(\mathbf{0},z) = m^{\mathrm{SB}}(Z) - \mu\left[\langle m^{\mathrm{SB}}(Z)\rangle + 3Z\langle Z' m^{\mathrm{SB}}(Z')\rangle\right] \tag{28}$$

$$\tilde{n}^{\mathrm{TB}}(\mathbf{0},z) = m^{\mathrm{TB}}(Z) - \mu\left[\langle m^{\mathrm{TB}}(Z)\rangle + \frac{6\phi_q(1-\mu)}{\phi_\tau^2}\langle Z' m^{\mathrm{SB}}(Z')\rangle\right] \tag{29}$$

with $\phi_q \equiv (qh/2)(K_2/K_3)$, $\phi_\tau \equiv (h/2)\sqrt{\gamma_1^\star f/K_3}$, $\gamma_1^\star \equiv \gamma_1(1-\mu)$ and $\mu \equiv \alpha_2^2/(\gamma_1\eta_c)$. The latter equations use the average operator $\langle u(Z')\rangle \equiv \int_{-1}^{1} u(Z')\frac{\mathrm{d}Z'}{2}$ defined for any function u. The modified eigenmode profiles must be the solution to the following eigenmode problem, as demonstrated in the ESI†:

$$\begin{pmatrix}\partial_Z^2 + \phi_\tau^2 & 2\phi_q\partial_Z\\ -2\phi_q\partial_Z & \partial_Z^2 + \phi_\tau^2\end{pmatrix}\begin{pmatrix}m^{\mathrm{SB}}(Z)\\ m^{\mathrm{TB}}(Z)\end{pmatrix} = \mathbf{0}, \tag{30}$$

I note that the variable μ was already introduced in Sec. 2 as the main backflow parameter, and was also used in previous publications[14]. This parameter must be in the half-open range $[0,1[$ according to the strict thermodynamic inequalities in eqn (17). The variable ϕ_τ^2 can be interpreted as a convenient renormalized decay frequency which simplifies the dispersion equations obtained in the following. This variable is directly proportional to the rescaled decay frequency introduced in the experimental Sec. 2 with dimensional analysis through the relation $\phi_\tau^2 = (\pi/2)^2(\tau_h/\tau)$. Similarly, $\phi_q = (\pi/2)(q/q_c) = (\pi/2)(C/C_c)$ can also be interpreted as the rescaled mass fraction of chiral molecules. These new variables are much more convenient because they typically appear as the arguments of cosine and sine functions, where the natural unit is the radian—hence the $\pi/2$ factors. The "average" terms in eqn (28,29) are a direct consequence of the boundary conditions induced by confinement in the z-direction. They describe the same effect as the one first revealed by Čopič *et al.*[14], but I stress that the formalism presented here is more general since it includes the coupling with chirality (term proportional to ϕ_q in eqn (29)).

Looking at eqn (30,28,29), one immediately observes that the SB and TB components must have opposite parity, i.e. either $\tilde{n}^{\mathrm{SB}}$ is even and $\tilde{n}^{\mathrm{TB}}$ is odd ("even-odd" case in the following), or conversely $\tilde{n}^{\mathrm{SB}}$ is odd and $\tilde{n}^{\mathrm{TB}}$ is even ("odd-even" case in the following) with respect to Z. The dispersion relation of the rescaled eigenvalue ϕ_τ^2 for each case can be found with a three-step calculation: search solutions of eqn (30) as sums of cosine and sine functions, write a linear system of equations associated with the zero-Dirichlet BCs for $\tilde{n}^{\mathrm{SB}}$ and $\tilde{n}^{\mathrm{TB}}$, and impose that the determinant of this system is zero to get non-trivial eigenmodes. The full calculation can be found in the ESI†, and leads to the following general form for the dispersion relation of both cases:

$$R_1(\phi_s)R_2(\phi_s) = \frac{3\mu\phi_q^2}{\phi_\tau^2}R_q(\phi_s), \tag{31}$$

with $\phi_s \equiv \sqrt{\phi_q^2 + \phi_\tau^2}$. The functions R_1 and R_2 are defined as follows:

$$R_1(\phi_s) \equiv \cos\phi_s - \mu\,\mathrm{sinc}\,\phi_s, \tag{32}$$

$$R_2(\phi_s) \equiv \begin{cases}\mathrm{sinc}\,\phi_s & \text{(even-odd mode)},\\ \left(1 - \frac{3\mu}{\phi_s^2}\right)\mathrm{sinc}\,\phi_s + \frac{3\mu}{\phi_s^2}\cos\phi_s & \text{(odd-even mode)}.\end{cases} \tag{33}$$

In an achiral sample, $\phi_q = 0$ and the dispersion relation is simply given by $R_1(\phi_\tau)R_2(\phi_\tau) = 0$, which can be checked to agree with the one derived with a different method by Čopič *et al.*[14]—who focused on the even-odd mode branch. In a cholesteric sample, chirality couples together the different mode branches through the function R_q, whose definition is longer than for $R_{1,2}$ and is therefore given in the ESI†.

By numerically solving eqn (31) to find the eigenvalue ϕ_τ and deducing the associated director profiles, I found that the eigenmodes can be uniquely identified by the index α of their dominant component ($\alpha = 0$ if $\max_z\left[\tilde{n}^{\mathrm{SB}}\right] > \max_z\left[\tilde{n}^{\mathrm{SB}}\right]$, else $\alpha = 1$) and the number m of inflexion points in the profile of their dominant component. In the following, the associated eigenvalues and profiles of eigenmode components will respectively be denoted by $\phi_\tau^{(\alpha,m)}$, $n^{(\mathrm{SB},\alpha,m)}$ and $n^{(\mathrm{TB},\alpha,m)}$ (dropping the tilde for simplicity). Fig. 6 shows the director profiles of the first fluctuation eigenmodes. Most importantly, one can directly check that when $\phi_q = \pi/2$, i.e. when the sample is at the threshold of destabilization of the unwound phase with $C = C_c$, the first two eigenvalues solution of eqn (31) are given by $\phi_\tau^{(0,0)} = \phi_\tau^{(1,0)} = 0$, with $\phi_\tau^{(0,0)}$ (resp., $\phi_\tau^{(1,0)}$) associated with an even-odd (resp., odd-even) mode profile. This demonstrates the theoretical existence of two soft modes with diverging decay times (or equivalently vanishing decay frequencies) at the onset of destabilisation of the sample. Using a Taylor series expansion of eqn (31) in $1-(C/C_c)^2$, I found that the rescaled decay frequencies $\tau_h/\tau^{(\alpha,0)} = \left[2\phi^{(\alpha,0)}/\pi\right]^2$ of these two soft modes have the following approximate expressions:

$$\frac{\tau_h}{\tau^{(\alpha,0)}} = \frac{(1-\mu)\left[1-(C/C_c)^2\right]}{1-\frac{\mu}{2}\left[f_\alpha(\mu) + g_\alpha(\mu)\,(C/C_c)^2\right]} \tag{34}$$

The functions f_α and g_α (with $\alpha = 0,1$) obtained from the Taylor series are given in the ESI†. By construction, they are associated with a very good asymptotic behaviour near $C = C_c$, but the accuracy is not so good near $C = 0$. To get a better fit function for the experiments, one can instead define these functions as first-order polynomials in the backflow parameter μ. By fitting with

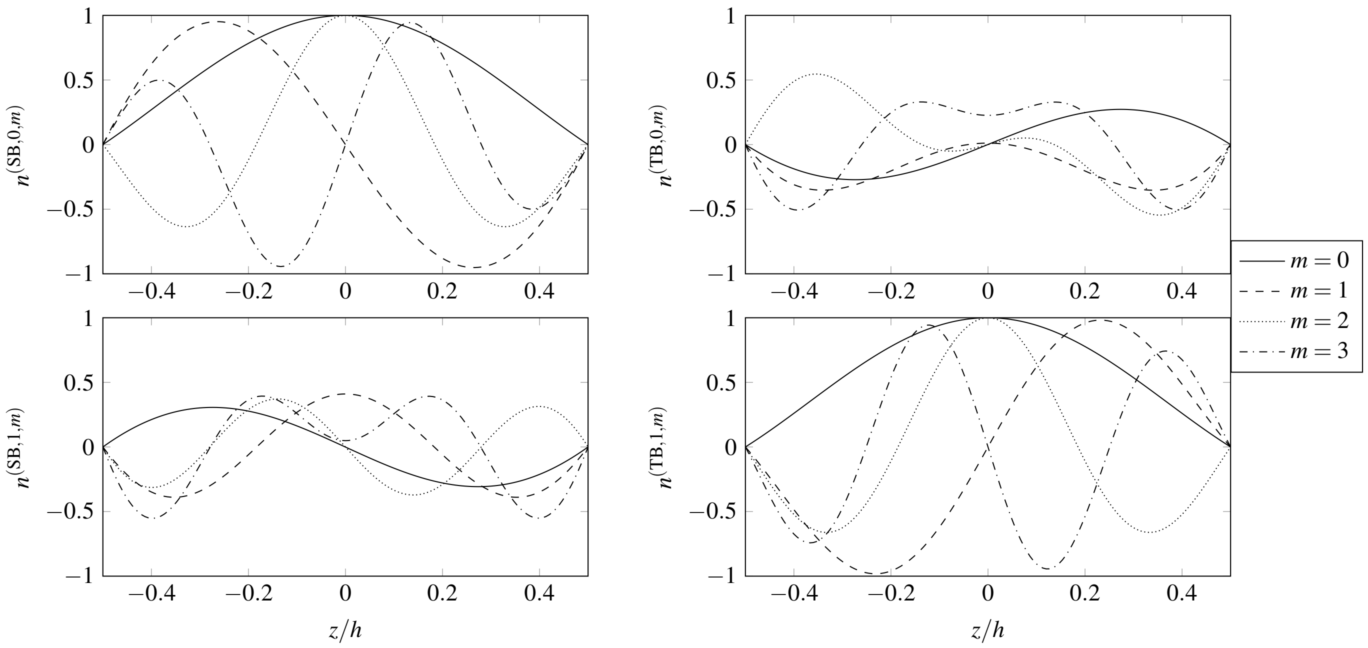

Fig. 6 Director profiles of the first fluctuation eigenmodes calculated in the limit $|\boldsymbol{k}_\perp| \to 0$ with the material constants of Table 1 and $C/C_c = 0.6$. Modes with dominant SB (TB) components are shown on top (bottom) and are ordered with the number m of inflexion points as explained in the main text.

eqn (34) the numerically calculated eigenvalues over the range $\mu \in [0,1[$ with $C=0$, I find the following expression for the functions f_α:

$$f_0(\mu) = f_1(\mu) = 0.3799 - 0.0247\mu, \qquad (35)$$

and by including the range $C \in [0, C_c]$ into the fit, I find the following expressions for the functions g_α:

$$g_0(\mu) = 0.6581 - 0.0342\mu, \qquad (36)$$

$$g_1(\mu) = 0.3212 + 0.0074\mu. \qquad (37)$$

The relative error between eqn (34) and the numerically calculated eigenvalues was found to be less than 0.08 % on average and implies that this fitting function is therefore well-suited for quantitative analysis of the experiments. I remark that the rescaled decay frequencies $\tau_h/\tau^{(0,0)}$ and $\tau_h/\tau^{(1,0)}$ have very similar values (within less than 10 %) and cannot be distinguished in the experiments due to the noise (at least with the setup used for this paper).

Before examining the case of eigenmodes with arbitrary $\boldsymbol{k}_\perp$, let us discuss an important point related to symmetries. An attentive reader surely must be surprised by now that the eigenmode profiles calculated in this section do not appear to agree with the rotational invariance around the z-axis when $\boldsymbol{k}_\perp = \boldsymbol{0}$. Indeed, a null transverse wavevector implies that the SB and TB axes $\boldsymbol{k}_\perp$ and $\boldsymbol{e}_z \times \boldsymbol{k}_\perp$ become arbitrary and should lead to rotationally invariant equations for the components of the director field. This is indeed the case of eqn (30) but not the case of eqn (28,29). The reason for this discrepancy is that the dissipation operators $\boldsymbol{\Gamma}^{\mathrm{SB}}$ and $\boldsymbol{\Gamma}^{\mathrm{TB}}$ do not have the same limit when $|\boldsymbol{k}_\perp| \to 0$. As a matter of fact, this already quite peculiar observation is accompanied by an even stranger divergence of the pressure under the same limit, as demonstrated in the ESI†. Such a divergence is unacceptable and hints that the incompressibility condition ceases to be valid at large wavelengths, for which large quantities of fluid are moved around by the thermal fluctuations. Taking into account the compressibility of the fluid (however weak it may be) leads to a crossover between incompressible dynamics at large wavevectors and compressible dynamics at small (but nonzero) wavevectors, and also gives the right rotational invariance of the modes when $\boldsymbol{k}_\perp = \boldsymbol{0}$. A rigorous demonstration of this result is not trivial and outside the scope of this paper, and will therefore be published in a separate paper.

However, I emphasize that this cross-over between compressible and incompressible dynamics is a mathematical subtlety that is likely inaccessible in most experiments. Indeed, to examine the effect of compressibility on a given fluctuation mode with relaxation time τ, let us use a simple isothermal state equation[30] $\kappa_T \partial_t P = (\partial_t \rho)/\rho$ with ρ the density and κ_T the isothermal compressibility (of the order of $0.6\,\mu\mathrm{m}^2/\mathrm{mN}$ in the isotropic phase of a common liquid crystal[31]). From the continuity equation $(\partial_t \rho)/\rho = -\boldsymbol{\nabla} \cdot \boldsymbol{v}$ and the compressible Stokes equation, one deduces that the flow becomes compressible when the transverse wavelength of the fluctuation mode is comparable to $\lambda_c \equiv h\sqrt{\tau/(\eta_a \kappa_T)}$. Taking $\tau \approx 0.1\,\mathrm{s}$ (experimental order of magnitude for the fundamental mode, see Fig. 2c) and $\eta_a \approx 33.2\,\mathrm{mPa\,s}$ (see Table 1), I estimate that $\lambda_c \approx 7\,10^5 h$, which by far is much larger than the sample lateral extent ($\sim 2\,\mathrm{cm}$) for typical thicknesses h of 1–100 μm. In experiments with finite-size samples, truly translationally invariant mode cannot exist and one can only observe modes with finite wavevector. Even the zero-frequency "fundamental" mode measured by DDM must include contributions from

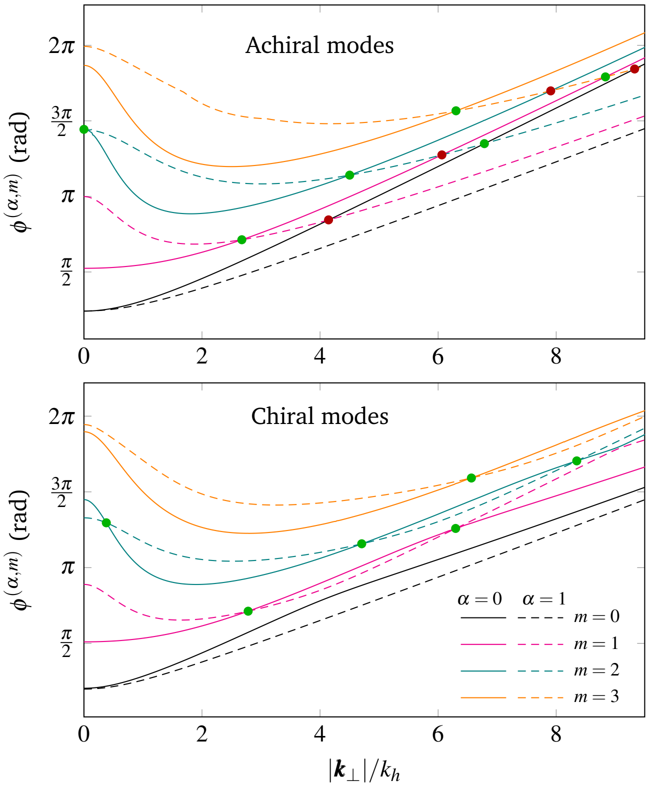

Fig. 7 Eigenvalues of the first fluctuations modes as a function of the rescaled transverse wavevector amplitude $|\boldsymbol{k}_\perp|/k_h$, calculated with the material constants of Table 1. The top (bottom) graph corresponds to achiral (chiral) modes calculated with $C=0$ ($C/C_c=0.6$). The legend applies to both graphs. Green points correspond to crossings (i.e. degeneracies of eigenmodes) present in both achiral and chiral systems. Conversely, red points correspond to crossings which are only present in achiral systems.

wavevectors of amplitudes between 0 and π/L (with $L\approx 167\mu$m the size of the observation windows in my experiments) since the DDM technique is based on a discretised and finite observation window. Thus, the fluctuation modes probed in the experiments of Sec. 2 are always measured for (effective) transverse wavevectors much bigger than the cross-over frequency π/λ_c, for which one can consider that the incompressibility condition is excellent.

3.2.3 Numerical calculation of modes with arbitrary transverse wavevector

For completeness, I also solved the eigenvalue problem in eqn (27) for general transverse wavevector $\boldsymbol{k}_\perp$. Although the dispersion relaxation can in principle be calculated with the same method as in the previous subsection, it is much more complicated. For this reason, I decided to use a numerical resolution based on a finite difference discretisation of eqn (27) accurate at order 2 in the mesh spacing. The actions of the matrix inverses in the dissipation operators are calculated with a standard Conjugate Gradient iterative solver until a relative accuracy of 10^{-10} is reached. The generalized eigenvalue problem is solved with a tolerance of 10^{-8} with the python library scipy[32], which interfaces the Implicitly Restarted Lanczos Method of the ARPACK library[33]. All results presented here were obtained by using the material constants of Table 1 and 151 discretisation points for the z-direction.

Fig. 7 shows the first eigenvalues as a function of the renormalized wavevector amplitude $|\boldsymbol{k}_\perp|/k_h$ (with $k_h\equiv\pi/h$) for achiral and chiral samples. This figure uses the same ordering convention as in the previous subsection and traces by continuity each mode branch from the eigenvalues calculated in the limit $|\boldsymbol{k}_\perp|\to 0$ (i.e. the eigenvalues of the previous subsection). A peculiar feature of this graph is that some crossings of achiral eigenvalues branches (highlighted with red points in the top graph of Fig. 7) are removed as soon as chirality is introduced in the system (contrary to the green crossings in Fig. 7, which are present both in achiral and chiral cases). The removal of these degeneracies is called an *avoided crossing* in the condensed matter community, and is similar to the opening of bandgaps in the optical band structure of photonic crystals when the permittivity contrast increases[34], and other related phenomena in condensed matter and quantum mechanics[35]. These avoided crossings always happen between two neighbouring branches $\phi^{(0,m)}$ and $\phi^{1,m\pm1}$, i.e. neighbouring branches with the same symmetry properties (they are both associated with even-odd or odd-even mode profiles). Interestingly, when looking at the mode profiles around avoided crossings, one observes that the number of inflexion points for one of the director components changes by 2, as illustrated in Fig. 8 for the lowest order branches. These mode transformations and avoided crossings are solely due to the symmetry breaking introduced by chirality, which couples together the two components of the director field. They are therefore fundamentally different from the ones already mentioned by Čopič *et al.*[14], which are rather due to the hydrodynamic boundary conditions in planar achiral samples.

4 Discussion

We can now discuss further the experimental results of Sec. 2 in light of the theoretical results of Sec. 3. Let us focus first on the measurement of the fundamental decay frequency. Since the DDM technique is based on spatially discretised intensity signals, this "fundamental" mode does not correspond exactly to $\boldsymbol{k}_\perp=\boldsymbol{0}$ but to a weighted average of all modes with wavevector amplitudes typically smaller than $2\pi/L$ with $L\approx 167\mu$m the lateral size of the experimentally observed region of interest[‡]. In particular, this means that the great majority of these modes are in the incompressible regime described at the end of Sec. 3.2.2, since L is much smaller than the critical wavelength λ_c associated with compressible effects.

On the other hand, L is also much bigger than the thickness h of the sample. We can therefore deduce from the theoretical results of Sec. 3 that the decay frequencies of these long-wavelength modes are all approximately described by eqn (34) with $\alpha=0$ or 1 depending on the (random) orientation of their wavevector with respect to the y-axis of the sample. One may therefore assume that our measurement of the fundamental decay frequency

---

[‡] This can be checked by calculating the zero-frequency coefficient of the discretised Fourier transform for a signal with arbitrary frequency k, and finding a weight of the form $\mathrm{sinc}(kL/2)N$ when the number of discretisation points N is high.

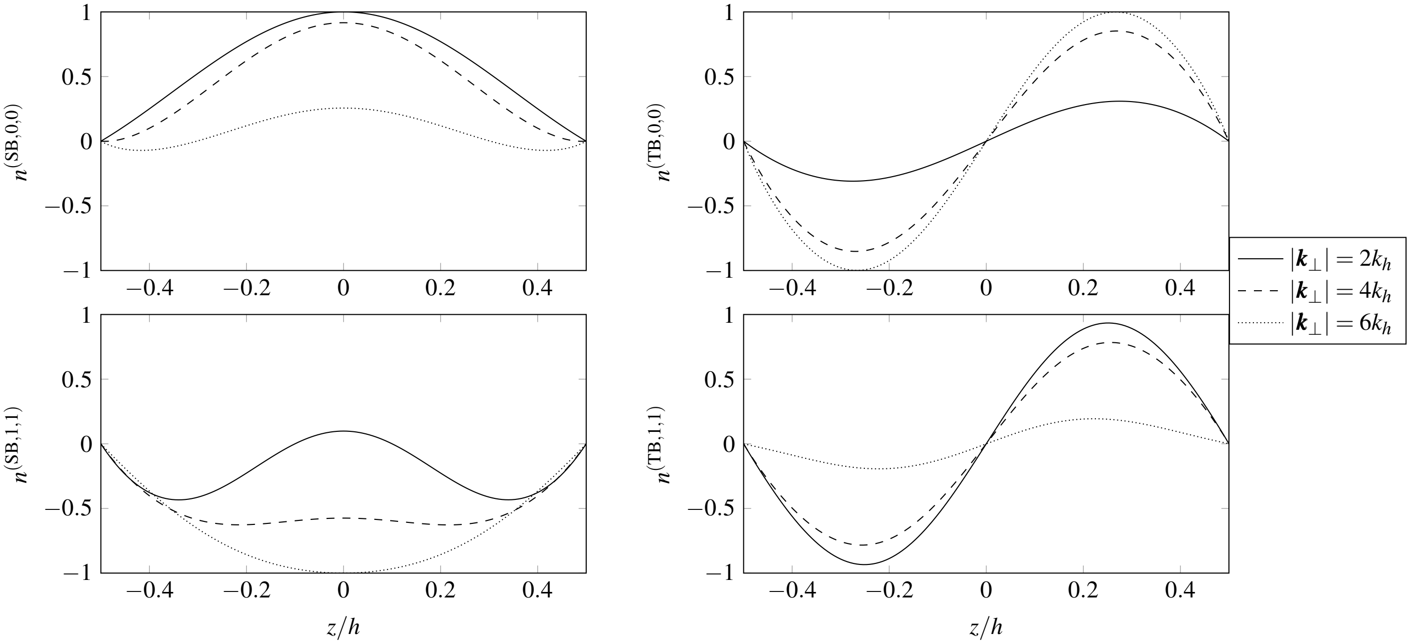

Fig. 8 Eigenmode profiles near the lowest red point of Fig. 7, which corresponds to a degeneracy of eigenmodes lifted by chirality. The top (bottom) graph shows the profiles associated with the branches $\{\alpha = 0, m = 0\}$ ($\{\alpha = 1, m = 1\}$). The same calculation parameters as in the bottom graph of Fig. 7 were used (material constants of Table 1 and $C/C_c = 0.6$).

corresponds to an average of the decay frequencies $\tau_h/\tau^{(0,0)}$ and $\tau_h/\tau^{(1,0)}$, which are too similar to be separated by a double-decay-time fit in my experiments as discussed in Sec. 3.2.2. This average is well-described by the experimental fit function in eqn (11) on condition to define the coefficients T_0 and T_1 as follows:

$$T_0 = \frac{1 - \frac{\mu f_0(\mu)}{2}}{1-\mu} = \frac{1 - \frac{\mu f_1(\mu)}{2}}{1-\mu} = \frac{1 - 0.1900\mu + 0.0171\mu^2}{1-\mu} \qquad (38)$$

$$T_1 = \frac{\mu(g_0(\mu) + g_1(\mu))}{4(1-\mu)} = \frac{0.2448\mu - 0.0067\mu^2}{1-\mu} \qquad (39)$$

To check the validity of these formulas, one can use the material constant values of Table 1 to calculate $\mu \approx 0.759$, from which we deduce $T_0^{\text{theory}} \approx 3.59$ and $T_1^{\text{theory}} \approx 0.75$. This value of T_0 agrees within $2\,\%$ with the fitted value of Sec. 2.4, but the predicted value of T_1 is quite far from the fitted value of 0.4. However, I emphasize that the fit gives a terrible accuracy of $\sim 75\,\%$ for the parameter T_1, which indicates that this parameter is much more sensitive to the experimental noise than the other parameters. Another way of checking the validity of these formulas is to fit again the experimental data in Fig. 3b, this time setting T_0 and T_1 to their predicted values T_0^{theory} and T_1^{theory} but allowing the HTP of the mixture to be a free parameter of the fit through the critical mass fraction of R811 C_c. With this procedure, I estimate HTP $= 0.1173 \pm 0.002\,\mathrm{wt\%}^{-1}\mu\mathrm{m}^{-1}$, which agrees within $1.6\,\%$ with the experimentally measured value of the HTP using a Cano wedge sample (see the beginning of Sec. 2).

In addition to the fundamental decay frequency, one may also try to compare the experimental dispersion curves plotted in Fig. 3c with the theoretical model. For this, we need first to clarify the selection rule presented in Sec. 2.2 which for simplicity was demonstrated in the case of nematic or weakly chiral samples. In Sec. 3, I showed that the director profiles of the chiral fluctuation modes were not defined in a single plane, but were associated with twisted director perturbations along both $\boldsymbol{e}_1 = \boldsymbol{k}_\perp/|\boldsymbol{k}_\perp|$ and $\boldsymbol{e}_2 = \boldsymbol{e}_z \times \boldsymbol{e}_2$. This means that in principle, the selection rule of Sec. 2.2 is not perfect in chiral samples, and there should exist an additional contribution $\delta S(\boldsymbol{k}_\perp)$ to the scattering cross-section, which should typically be proportional to the squared spontaneous wavevector and select the opposite eigenmodes than in eqn (4) along the x and y axes. If δS becomes non-negligible, it should therefore be associated with a second decay time in the DDM signal, since we showed that the rescaled decay frequencies $\tau_h/\tau^{(1,0)} \equiv \left[2\phi^{(1,0)}/\pi\right]^2$ and $\tau_h/\tau^{(0,0)} \equiv \left[2\phi^{(0,0)}/\pi\right]^2$ are different. Using the numerical package *pyReSpect*[36], I extracted the continuous spectrum of decay times from the DDM signals in my most chiral samples and found that in the range of studied wavevectors, there is only a single peak in this spectrum with its maximum matching the decay time fitted with the simple one-decay-time law. We can therefore neglect the cross-contribution δS in our setup, and assume that the selection rule of Sec. 2.2 is still valid in cholesterics, at least within the accuracy of the setup of Fig. 1a.

Accordingly, the dispersion curves in the left (resp., right) plot Fig. 3c should be calculated from the quantity $\tau_h/\tau^{(1,0)}$ (resp., $\tau_h/\tau^{(0,0)}$) of our theoretical model. The shape of these dispersion curves is mainly determined by the elastic constant ratios K_1/K_3 and K_2/K_3. I already showed that the measurements of the fundamental decay frequencies were compatible with the theory of Sec. 3 when the values of μ, τ_h and K_2/K_3 were calculated from the material constants in Table 1, so we can safely assume that the values of K_2, K_3 and the viscosities in Table 1 are accurate. I therefore numerically calculated the dispersion curves (plain lines in Fig. 3c) keeping only K_1/K_3 as a free parameter. The best fit between experiments and theory was obtained when $K_1/K_3 \approx 0.74$, which is only $\sim 4\,\%$ smaller than the value estimated from Table 1. We may therefore conclude that the theoretical model of Sec. 3 provides a reliable model of the critical relaxation of fluctuation modes in confined cholesterics.

5 Conclusion

To summarise, the dynamic and static properties of fluctuation modes in unwound cholesteric samples were experimentally characterized with the DDM technique and compared to a theoretical model allowing the calculation of the decay frequencies of all confined fluctuation modes. The most important result of this paper is the combined experimental and theoretical evidence of two soft modes of fluctuations driving the destabilization transition of the unwound state, with associated divergences of both decay times and correlation lengths. The critical behaviours characterized here are very similar to the ones observed in usual thermodynamic phase transitions[37], except here the transition is of structural type and is driven by an intricate balance between chirality and confinement. At a fundamental level, the unwound director field of a confined cholesteric sample corresponds to a very high level of frustration of the cholesteric phase, which has removed any traces of chirality from its equilibrium state. Despite this, the experiments presented here demonstrate that chirality is hidden in the orientational fluctuations of the LC around the equilibrium state and still plays a major role in the dynamics of this system by modulating the decay times of fluctuation modes.

One of the most intriguing consequences of this work is the possibility of measuring the rescaled spontaneous twist q/q_c of a cholesteric in unwound samples instead of Cano wedge samples, simply by measuring the decay time of the fundamental fluctuation mode and using eqn (11) with $C/C_c = q/q_c$. Such a measurement is of course less direct than the Cano wedge technique since it necessitates the knowledge of the backflow parameter μ and of the typical decay time τ_h (both of which can be directly measured in a nematic sample), but has the major advantage of being an in-situ measurement. This may prove advantageous to characterize the strength of chirality in frustrated cholesteric samples embedding isolated topological solitons such as cholesteric bubbles (also called torons) or fingers for light flow manipulation[38,39], thus allowing supporting simulations of these structures to be run with adequate parameters for comparison with experiments.

Another straightforward extension of this work would be to analyse the same chirality-driven critical behaviours in more complicated frustrated states of the cholesteric phase, such as the translationally-invariant configuration (TIC) or the periodic cholesteric finger pattern[19]. For example, one could use a chiral LC mixture with a negative dielectric anisotropy and tune the dynamics of the fluctuation modes using an electric field to drive the second-order transition between unwound cholesteric and TIC, assuming a sample thickness below the triple point[40]. The advantage of such a system is that below the triple point, fingers are always unstable and therefore cannot break the translational invariance of the sample—contrary to the highly chiral samples of this study.

Conflicts of interest

There are no conflicts to declare.

Acknowledgements

The author acknowledges financial support from the CNRS and the INP, and warmly thanks Luca Cipeletti for discussions about DLS/DDM, and Christophe Blanc and Patrick Oswald for their critical reading of the paper and valuable comments on confined hydrodynamics, LC experiments and cholesteric finger stability.

References

1 B. J. Berne and R. Pecora, *Dynamic light scattering: with applications to chemistry, biology, and physics*, Dover, New York, 2000.

2 R. Borsali, R. Borsali and R. Pecora, *Soft-matter characterization*, Springer, Berlin, 2008.

3 K. N. Pham, A. M. Puertas, J. Bergenholtz, S. U. Egelhaaf, A. Moussaıd, P. N. Pusey, A. B. Schofield, M. E. Cates, M. Fuchs and W. C. Poon, *Science*, 2002, **296**, 104–106.

4 L. Cipelletti, L. Ramos, S. Manley, E. Pitard, D. A. Weitz, E. E. Pashkovski and M. Johansson, *Faraday discussions*, 2003, **123**, 237–251.

5 V. Nigro, B. Ruzicka, B. Ruta, F. Zontone, M. Bertoldo, E. Buratti and R. Angelini, *Macromolecules*, 2020, **53**, 1596–1603.

6 G. Del Monte, D. Truzzolillo, F. Camerin, A. Ninarello, E. Chauveau, L. Tavagnacco, N. Gnan, L. Rovigatti, S. Sennato and E. Zaccarelli, *Proceedings of the National Academy of Sciences*, 2021, **118**, e2109560118.

7 Z. Yu, J. C. Reid and Y.-P. Yang, *Journal of pharmaceutical sciences*, 2013, **102**, 4284–4290.

8 M. Dahesh, A. Banc, A. Duri, M.-H. Morel and L. Ramos, *The Journal of Physical Chemistry B*, 2014, **118**, 11065–11076.

9 A. Y. Val'kov, V. P. Romanov and A. Shalaginov, *Physics-Uspekhi*, 1994, **37**, 139.

10 G.-P. Chen, H. Takezoe and A. Fukuda, *Liquid Crystals*, 1989, **5**, 341–347.

11 M. Cui and J. R. Kelly, *Molecular Crystals and Liquid Crystals Science and Technology. Section A. Molecular Crystals and Liquid Crystals*, 1999, **331**, 49–57.

12 A. Mertelj and M. Čopič, *Physical Review Letters*, 1998, **81**, 5844–5847.

13 I. D. Olenik, M. Jazbinšek and M. Čopič, *Physical Review Letters*, 1999, **82**, 2103–2106.

14 M. Čopič, M. Vilfan and A. Mertelj, *Liquid Crystals*, 2013, **40**, 1646–1654.

15 Z. Parsouzi, S. M. Shamid, V. Borshch, P. K. Challa, A. R. Baldwin, M. G. Tamba, C. Welch, G. H. Mehl, J. T. Gleeson, A. Jakli, O. D. Lavrentovich, D. W. Allender, J. V. Selinger and S. Sprunt, *Physical Review X*, 2016, **6**, 021041.

16 J. Pišljar, S. Ghosh, S. Turlapati, N. Rao, M. Škarabot, A. Mertelj, A. Petelin, A. Nych, M. Marinčič, A. Pusovnik *et al.*, *Physical Review X*, 2022, **12**, 011003.

17 M. Giridhar and K. Suresh, *The European Physical Journal E*, 2002, **7**, 167–173.

18 L. L. Jia, M. J. Zakhary, Z. Dogic, R. A. Pelcovits and T. R. Powers, *Physical Review E*, 2017, **95**, 060701.

19 P. Oswald and P. Pieranski, *Nematic and Cholesteric Liquid Crystals: Concepts and Physical Properties Illustrated by Experiments*, CRC Press, Boca Raton, 2006.

20 J.-S. B. Tai and I. I. Smalyukh, *Science*, 2019, **365**, 1449–1453.

21 P. J. Ackerman and I. I. Smalyukh, *Physical Review X*, 2017, **7**, 011006.

22 F. Giavazzi, S. Crotti, A. Speciale, F. Serra, G. Zanchetta, V. Trappe, M. Buscaglia, T. Bellini and R. Cerbino, *Soft Matter*, 2014, **10**, 3938–3949.

23 B. Y. Zel'dovich and N. V. Tabiryan, *Journal of Experimental and Theoretical Physics*, 1981, 5.

24 P.-G. De Gennes and J. Prost, *The Physics of Liquid Crystals*, Oxford university press, Oxford, 1993.

25 J. Korger, T. Kolb, P. Banzer, A. Aiello, C. Wittmann, C. Marquardt and G. Leuchs, *Optics Express*, 2013, **21**, 27032–27042.

26 F. Giavazzi and R. Cerbino, *Journal of Optics*, 2014, **16**, 083001.

27 F. Giavazzi, D. Brogioli, V. Trappe, T. Bellini and R. Cerbino, *Physical Review E*, 2009, **80**, 031403.

28 E. Guyon, R. Meyers and J. Salan, *Molecular Crystals and Liquid Crystals*, 1979, **54**, 261–272.

29 F. Brochard, P. Pieranski and E. Guyon, *Physical Review Letters*, 1972, **28**, 1681–1683.

30 H. Pleiner and H. R. Brand, *Pattern Formation in Liquid Crystals*, Springer New York, 1996, pp. 15–67.

31 J. Bendler, *Molecular Crystals and Liquid Crystals*, 1977, **38**, 19–30.

32 P. Virtanen, R. Gommers, T. E. Oliphant, M. Haberland, T. Reddy, D. Cournapeau, E. Burovski, P. Peterson, W. Weckesser, J. Bright *et al.*, *Nature methods*, 2020, **17**, 261–272.

33 R. B. Lehoucq, D. C. Sorensen and C. Yang, *ARPACK users' guide: solution of large-scale eigenvalue problems with implicitly restarted Arnoldi methods*, SIAM, 1998.

34 *Photonic Crystals: Molding the Flow of Light*, ed. J. D. Joannopoulos, Princeton University Press, Princeton, 2nd edn, 2008.

35 N. W. Ashcroft and N. D. Mermin, *Solid state physics*, Saunders College Publishing, New-York, 1976.

36 S. Shanbhag, *Macromolecular Theory and Simulations*, 2019, **28**, 1900005.

37 P. M. Chaikin, T. C. Lubensky and T. A. Witten, *Principles of condensed matter physics*, Cambridge university press Cambridge, 1995, vol. 10.

38 A. J. Hess, G. Poy, J.-S. B. Tai, S. Žumer and I. I. Smalyukh, *Physical Review X*, 2020, **10**, 031042.

39 G. Poy, A. J. Hess, Andrew J. Seracuse, M. Paul, S. Žumer and I. I. Smalyukh, *Nature Photonics*, 2022, **16**, 454.

40 P. Ribiere, S. Pirkl and P. Oswald, *Physical Review A*, 1991, **44**, 8198.